Acousto-optical interaction and its advanced applications

By:

Phys. Adán Omar Arellanes Bernabe

A dissertation Submitted to the program in Optics.

Optics department.

In partial fulfillment of the requirements for the degree of

MASTER IN SCIENCES WITH SPECIALITY OF OPTICS

At:

National Institute for Astrophysics, Optics, and Electronics.

August 2013

Tonantzintla, Puebla.

Advisor:

Dr. Alexander S. Shcherbakov

INAOE Researcher

Optics Department

Contents

To my family

Acknowledgements

I thank to all the Mexican people who, through CONACyT, makes possible all the scientific development, including this thesis, in our country

I thank my advisor Dr. Alexander Shcherbakov for sharing all his experience and knowledge, both scientific and personal.

Thanks to the INAOE for giving me all the knowledge to makes this work possible.

Thanks to my co-authors Dr. Vahram Chavushyan and Dr. Sergey A. Nemov.

Thanks to my examiners Dr. David Sánchez de la Llave and Dr. Mauro Sánchez Sánchez for their help and support.

Thanks to all my professors and specially Dr. Ponciano Rodriguez, Dr. Victor Arrizon, Dr. Eugene Kuzin, Dr. Baldemar Ibarra, Dr. Sabino Chavez, and Dr. Nikolai Korneev.

Also thanks to my colleagues and friends Gabriel Mellado, César Camacho, Josué Peralta, Noemí Sánchez, Ana V. Hanessian, Fabián Villa, Mayra Vargas, and Jesús Arriaga for all their support and company during my studies.

Special thanks to my parents Adán Arellanes and Noemí Bernabe, and to my sisters Diana, Patricia and Julia for their love and support.

Abstract

In this this work, the acousto-optical interaction is studied. Since its inception, in 1922, it has been widely studied and applied. Here, the development of three advanced application of this branch of physics is considered.

First, is analyzed the potential use of an acousto-optical cell for be included as a dynamic diffraction grating, in order to improve in many ways the actual static gratings used, in the Guillermo Haro astrophysical observatory. For this, it was necessary to estimate the performance of several acousto-optical materials available today.

Second, a specific mechanism of the acousto-optical nonlinearity is studied to regulate the performance of the collinear acousto-optical filter. The theory of this phenomenon is analyzed and confirmed experimentally using and advanced filter based on calcium molybdate ($CaMoO_4$) single-crystal. The transmission function of electronically tunable filter exhibits a dependence on the applied acoustic power density, and as a result, it is possible to squeeze the transmission function at the cost of decreasing the device efficiency partially.

And at final, the triple product processor is studied for its potential application in spectroscopy designed for 3-inch optics and analyzing all the materials needed for its realization. The need to use 3-inch optics is mainly oriented to exploit an acousto-optical cells with large aperture windows to get a large time-bandwidth product.

Resumen

En este trabajo se estudia la interacción acusto-óptica. Desde sus comienzos en 1922 ha sido estudiada y aplicada ampliamente . Aquí están desarrolladas tres aplicaciones avanzadas de esta rama de la física.

Primero, se analiza el uso potencial de una celda acusto-óptica para ser incluida como una rejilla de difracción dinámica, con el fin de mejorar en varios aspectos las rejillas que se usan actualmente en el observatorio astrofísico Guillermo Haro en Cananea. Para esto fue necesario estimar el desempeño de varios materiales acusto-ópticos disponibles en la actualidad.

Segundo, un mecanismo específico de la nolinealidad acusto-óptica es estudiado para regular el desempeño de un filtro acusto-óptico colineal. La teoría de este fenómeno es analizada y posteriormente confirmada experimentalmente usando un filtro basado en un solo cristal de molibdato de calcio ($CaMoO_4$). La función de transmisión del filtro sintonizable electrónicamente muestra una dependencia en la densidad de potencia acústica aplicada, y como resultado, es posible estrechar la función de transmisión con la desventaja de disminuir parcialmente la eficiencia del aparato.

Y por último se estudia un procesador de triple producto para su potencial aplicación en espectroscopía, diseñado para un arreglo óptico de 3 pulgadas, analizando los materiales necesarios para su realización. La necesidad de usar el arreglo óptico de 3 pulgadas está principalmente orientado para explotar una celda acusto-óptica con una larga ventana de apertura para obtener un producto tiempo-ancho de banda grande.

Introduction

The acousto-optics is a branch of physics which joints the light phenomena with the sound and ultrasound phenomena. The study of the interaction between light and acoustic waves was first predicted by Brillouin in 1922 and later, this idea was refined by Debye and Sears in 1932, and by Lucas and Biquard. It continued with the investigations of Raman and Nath between 1935 and 1936. A heuristic physical approach was later proposed by Van Cittert in 1937 and many more contributions were made in the theoretical explanation of the phenomenon by many authors. Later, with the invention of the laser in 1960, a new need for controlling the light was born and more developments were made in acousto-optical applications and theory as well.

From deflection, filtering, and frequency shifting to parallel optical processing for the study of signals, the acousto-optics has never stopped in its development and has been used for several important experiments, for example, the first Bose-Einstein condensate in 1995. It has also been widely applied for spectroscopy in astrophysics, in filtering and acousto-optical signal processing.

Preface

The study of acousto-optical interaction is widely discussed within this thesis. Also, the development of new applications using this discipline is analyzed. The main motivation for this matter is its use in astrophysical spectroscopy but it is not limited to this area.

The first chapter is a very extensive introduction to acousto-optics, explaining the nature of acoustical and optical waves in order to establish the basic knowledge to understand the interaction between these two physical phenomena. Some concepts of the propagation of these waves in a medium are also explained.

In chapter number two, the design of a novel acousto-optical spectrometer for the Guillermo Haro astrophysical observatory is discussed. The analysis for the design of an acousto-optical cell for this spectrometer is also considered and some estimations of its potential performance were made.

In the third chapter a specific mechanism in the non-linear regime of acousto-optical interaction is discussed for its use in a collinear acousto-optical tunable filter to control its transmission function with the use of acoustic waves of finite amplitude.

The chapter four is directed to the analysis of the potential improvement of a triple product processor using 3-inch optics components in order to exploit the advantages for the time and space integration combined.

In the chapter five, the general conclusions of this thesis are presented.

Finally, some future work, related to the work developed in this thesis, is presented.

Chapter 1

Acousto-Optics

In this chapter, the basic theory of the acousto-optical interaction and generally some of the most used applications are presented [1.1] in order to set up the knowledge for the more recent and advanced applications. To understand this better, first is explained the behavior of the light in anisotropic media, then the propagation of sound in some medium and finally the interaction of these 2 phenomena.

1.1. Light Propagation in Anisotropic Media

The study of the propagation of light could be divided in two cases: isotropic and anisotropic. In an isotropic media the induced polarization is always parallel to the electric field and it is proportional to the susceptibility and this relation is independent to the direction of the applied field. It becomes more interesting for anisotropic media, where depending on the direction of the light in the media and its state of polarization, the induced polarization would change.

1.1.1. Index Ellipsoid and Surfaces.

Two different concepts must be introduced, which will allow the work mathematically and help visualize the differences between each type of crystals that will be used. In one hand it is the *index ellipsoid* which is defined as [1.2]

$$\frac{x^2}{\varepsilon_{xx}}+\frac{y^2}{\varepsilon_{yy}}+\frac{z^2}{\varepsilon_{zz}}=1, \tag{1.1}$$

where ε_{ii} are the components of the main diagonal in the dielectric tensor ε, and knowing that

$$n=\sqrt{\varepsilon\mu} \tag{1.2}$$

$\mathbf{n}$ is the refractive index and $\boldsymbol{\mu}$ the magnetic permeability which is effectively unity for all the materials are concerned for this thesis. Now it is possible to rewrite (1.1) into

$$\frac{\mathbf{x}^2}{\mathbf{n}_x^2}+\frac{\mathbf{y}^2}{\mathbf{n}_y^2}+\frac{\mathbf{z}^2}{\mathbf{n}_z^2}=\mathbf{1}. \tag{1.3}$$

As an example, let $\mathbf{n}_x=\mathbf{n}_y=\mathbf{n}_o$, $\mathbf{n}_z=\mathbf{n}_e$, and let $\mathbf{n}_o>\mathbf{n}_e$ so Eq.(1.3) becomes

$$\frac{\mathbf{x}^2+\mathbf{y}^2}{\mathbf{n}_o^2}+\frac{\mathbf{z}^2}{\mathbf{n}_e^2}=\mathbf{1}, \tag{1.4}$$

with this spheroid in mind, consider the wave vector $\vec{\mathbf{k}}$ in the direction of an arbitrary angle $\boldsymbol{\theta}$ to the $\mathbf{z}-$axis, then any plane that touches the origin and that is perpendicular to this wave vector will intersect the spheroid in an ellipse, see Fig. 1.1, which will have the following properties:

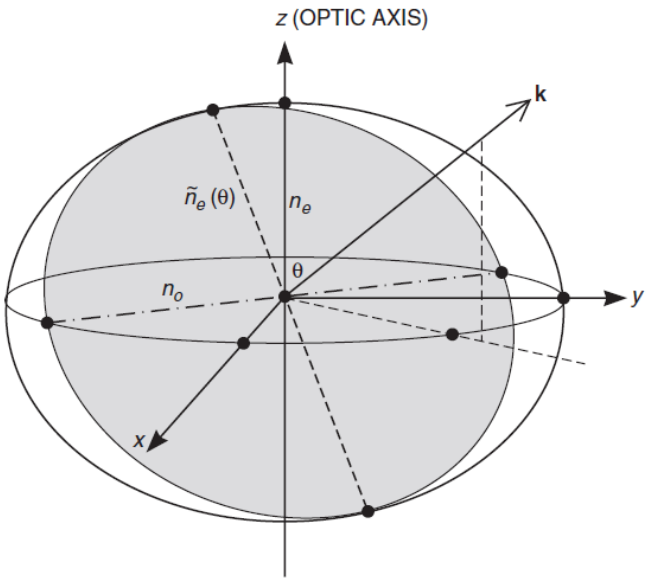

Figure 1.1 The index ellipsoid for a uniaxial medium. The shaded ellipse is perpendicular to the $\vec{\mathbf{k}}$ vector

1) The axes of this ellipse define two orthogonal directions for the electric displacement $\vec{\mathbf{D}}$ which satisfy simultaneously the Maxwell's equations and the constitutive relation

$$\vec{\mathbf{D}}=\boldsymbol{\varepsilon}_0\boldsymbol{\varepsilon}\vec{\mathbf{E}}. \tag{1.5}$$

one of the two axes is always in the $\mathbf{x}-\mathbf{y}$ plane and correspond to the direction of polarization of the ordinary wave and its length is independent of the direction of $\vec{\mathbf{k}}$. The other axes is related to the extraordinary wave and its length depends on the angle $\boldsymbol{\theta}$ between $\vec{\mathbf{k}}$ and the $\mathbf{z}-$axis.

2) The length of the semi-axis of the ellipse are the refractive indices, $\mathbf{n_o}$ for the ordinary wave and $\tilde{\mathbf{n}}_\mathbf{e}(\boldsymbol{\theta})$ for the extraordinary wave. The value of $\tilde{\mathbf{n}}_\mathbf{e}(\boldsymbol{\theta})$ is easily estimated from Fig. 1.2. The length of the bold line perpendicular to $\mathbf{k}$ in Fig. 1.2 is the value of

$$\tilde{\mathbf{n}}_\mathbf{e}(\boldsymbol{\theta}) = \sqrt{\frac{\cos^2\boldsymbol{\theta}}{\mathbf{n_o^2}} + \frac{\sin^2\boldsymbol{\theta}}{\mathbf{n_e^2}}}\,. \tag{1.6}$$

On the other hand there are the *index surfaces* which represent the values of the refractive indices for all the possible directions of propagation of the wave vector $\vec{\mathbf{k}}$.

Using the previous example, the index surface would look like Fig. 1.3b or 1.3c. The planes of polarization for the ordinary and extraordinary are perpendicular, this characteristic will be particularly useful for some applications listed in subsection 1.5.
The present work is focused on this representation and it will be explained for the different crystal types in the next section.

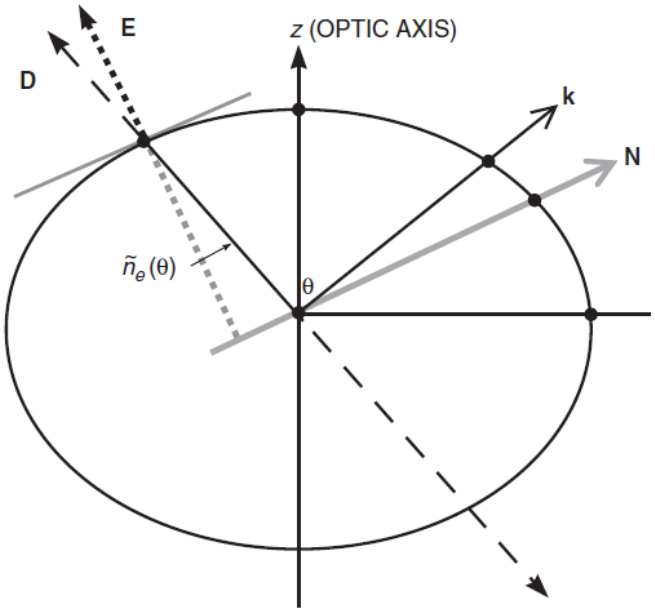

Figure 1.2 Projection of the index ellipsoid into the $\mathbf{k}-\mathbf{z}$ plane.

1.1.2. Crystals; Optically Isotropic, Uniaxial and Biaxial

In crystals, the optical isotropy is observed in cubic crystal systems (also applicable for amorphous media), in these systems the dielectric tensor $\boldsymbol{\varepsilon}$ is given by

$$\boldsymbol{\varepsilon} = \varepsilon_0 \begin{pmatrix} \mathbf{n^2} & \mathbf{0} & \mathbf{0} \\ \mathbf{0} & \mathbf{n^2} & \mathbf{0} \\ \mathbf{0} & \mathbf{0} & \mathbf{n^2} \end{pmatrix}, \tag{1.7}$$

where ε_0 is the permittivity of vacuum. In Fig. 1.3a is shown the expected index surface for this case which is the simplest one.

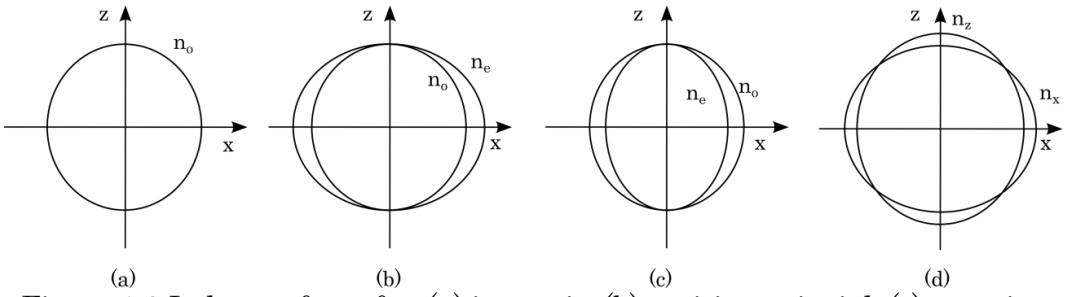

Figure 1.3 Index surfaces for: (a) isotropic, (b) positive uniaxial, (c) negative uniaxial, and (d) biaxial medium.

There also exist the uniaxial crystals; these ones are crystals systems of tetragonal, hexagonal and trigonal kind. Their dielectric tensor is of the form:

$$\varepsilon = \varepsilon_0 \begin{pmatrix} n_o^2 & 0 & 0 \\ 0 & n_o^2 & 0 \\ 0 & 0 & n_e^2 \end{pmatrix}, \tag{1.8}$$

being n_o the ordinary and n_e the extraordinary refractive index. In Fig. 1.3b and 1.3c it is seen the two cases for its index surface, if $n_e > n_o$ it is called 'positive uniaxial' and if $n_e < n_o$ it is called 'negative uniaxial'.

The biaxial crystals represent the most complicated case. The index surfaces for this type of crystal is shown in Fig. 1.3d. Its dielectric tensor is represented as

$$\varepsilon = \varepsilon_0 \begin{pmatrix} n_x^2 & 0 & 0 \\ 0 & n_y^2 & 0 \\ 0 & 0 & n_z^2 \end{pmatrix}. \tag{1.9}$$

1.2. Ultrasound Propagation in Anisotropic Media

The acoustic propagation is much more complicated than the light propagation, in the light wave what oscillates is the electromagnetic field but in the acoustic waves are the positions of the atoms/molecules.

Strain tensor

This tensor is related to the deformation of a body. In some coordinate system the position of any point is defined by a vector $\vec{r}(x = x_i, y = x_2, z = x_3)$. When the body is deformed this position changes to a new vector $r'(x'_i)$, and this displacement is given by the vector $\vec{u} = \vec{r}' - \vec{r}$;

$$u_i = x'_i - x_i, \tag{1.10}$$

which is called the displacement vector. When a body is deformed, the distance between two points will change. Let us consider two very close points with the radius vector joining the points as dx_i, the vector joining this points when deformed will be $dx'_i = dx_i + du_i$. Here the squared distance between the points is $dl^2 = dx_i^2$ before the deformation and $dl'^2 = dx'^2_i = (dx_i + du_i)^2$ after the deformation. Now $du_i = (\partial u_i / \partial x_k) dx_k$ is substituted to rewrite

$$dl'^2 = dl^2 + 2\frac{\partial u_i}{\partial x_k} dx_i dx_k + \frac{\partial u_i}{\partial x_k}\frac{\partial u_i}{\partial x_l} dx_k dx_l ,$$

the second term on the right can be rewritten as

$$\left(\frac{\partial u_i}{\partial x_k} + \frac{\partial u_k}{\partial x_i}\right) dx_i dx_k .$$

and then, in the third term the suffixes i and l are interchanged so

$$dl'^2 = dl^2 + 2u_{ik} dx_i dx_k , \tag{1.11}$$

where the tensor u_{ik} is defined as

$$u_{ik} = \frac{1}{2}\left(\frac{\partial u_i}{\partial x_k} + \frac{\partial u_k}{\partial x_i} + \frac{\partial u_l}{\partial x_k}\frac{\partial u_l}{\partial x_k}\right). \tag{1.12}$$

u_{ik} is called the strain tensor. This tensor represents the change in the distance between two points when a body is deformed. In this case, the body is a crystal and the deformation is caused by the acoustic wave. It is easy to see, from Eq. (1.12), the symmetry of the strain tensor,

$$u_{ik} = u_{ki} . \tag{1.13}$$

Because of this symmetry the strain tensor can be diagonalized at any given point. When diagonalized at a given point, the element of length, Eq. (1.11), becomes

$$dl'^2 = (1 + 2u^{(1)})\, dx_1^2 + (1 + 2u^{(2)})\, dx_2^2 + (1 + 2u^{(3)})\, dx_3^2 ,$$

where $u^{(i)}$ is the component of the diagonal of u_{ii}. From this expression is possible to see that the strain tensor is the sum of three independent directions mutually perpendicular.

1.2.1. Pure Longitudinal Waves

In these waves the direction of propagation of energy is in the same direction as the direction of the perturbation and only in this direction, Fig. 1.4a, generating zones of greater pressure traveling along the media.

In terms of the strain tensor, this wave is traveling in the same direction as the diagonalized strain tensor

1.2.2. Pure Shear Waves

Now the acoustic wave, in contrast with the longitudinal wave, makes the oscillation of the particles perpendicular to the direction of propagation, see Fig. 1.4b. Shear waves are slower than longitudinal waves and this will make them very useful for the acousto-optical applications explained later.

In terms of the strain tensor, this wave is traveling perpendicular to the direction of $\mathbf{u_{ii}}$.

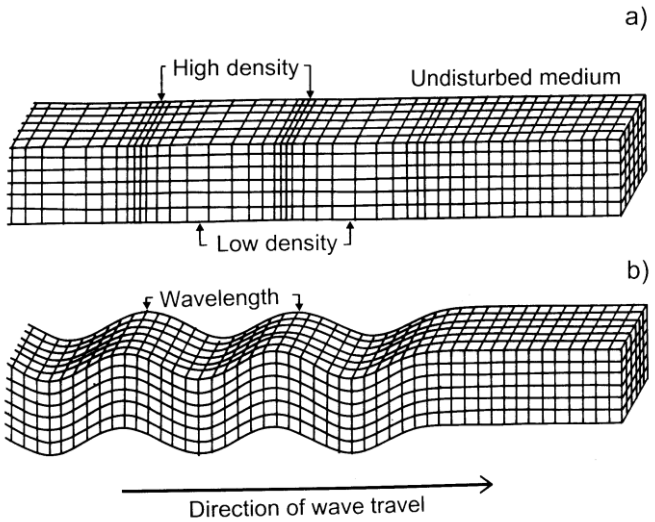

Figure 1.4 Acoustic waves in a medium; (a) pure longitudinal wave and (b) pure shear wave.

1.3. Acousto-Optical Interactions

This phenomenon occurs when the light propagates through a media which is under the action of acoustic waves (sound or ultrasound).
One approach for explaining this phenomenon is the next one: it is known that the sound is a perturbation which causes a difference in the pressure of the media where it travels. This perturbation produce a change in the refractive index of the material and, because of the periodicity of the acoustic wave, it creates a phase grating, see Fig. 1.5, which will be the responsible for the light to be diffracted. The parameters of this grating will be entirely determined by the intensity and the frequency of the acoustic wave.

The other approach comes from the quantum electrodynamics where the light will be treated like photons and the sound as phonons in a given field approximation, so the scattering will be caused when one photon absorbs one or more phonons and, because of the conservation of momentum, the photons will change their direction. To make it more clear, and get a deeper understanding of the phenomenon, the wave vector diagrams are introduced.

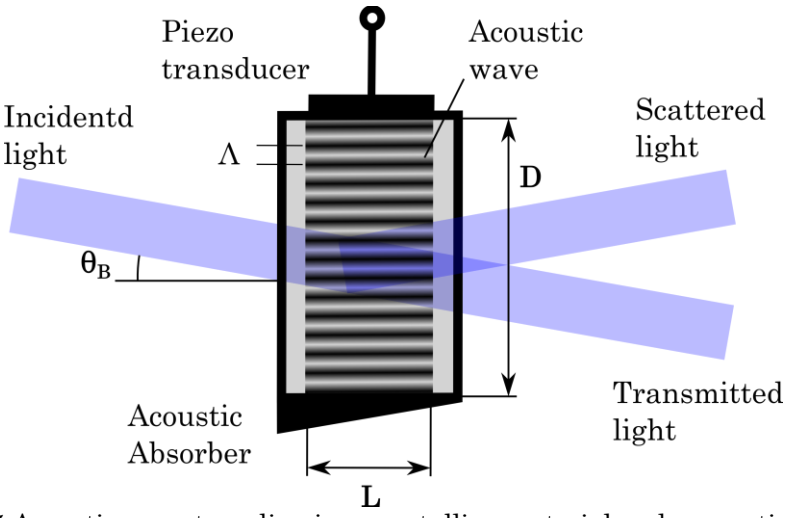

Figure 1.5 Acoustic wave traveling in a crystalline material and generating a phase grating. L is the interaction length, D is the aperture of the cell, Λ is the acoustic wavelength, and θ_B is the Bragg angle.

1.3.1. Wave Vector Diagrams; Normal and Anomalous Light Scattering

Let a set of interacting particles N_1 and N_2 of two fields exist, where N_1 is the field of interest, Fig 1.6, if $N_1 \approx N_2$ it is said that is in the regime of strong interaction (coupled fields), after the interaction, both fields are considerably affected.

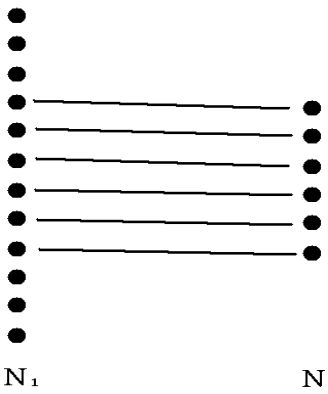

Figure 1.6 Two sets of interacting particles from an arbitrary field.

If $N_1 >> N_2$ it is called weak interaction because the field of N_1 is barely affected after the interaction. If $N_1 << N_2$ it is the so called given field approximation, where all the N_1 particles are interacting with the N_2. The number of N_2 particles is so large that after the interaction the field of N_2 is not even affected. The last one is the case for the acousto-optic interaction. Suppose one acoustic field and one optic field of the same intensity, the energy of each particle is given by

$$E = \hbar \omega, \tag{1.14}$$

where $\hbar$ is the Planck constant divided by 2π and ω is the frequency of the particle. For the photons $\omega_L \approx 10^{14}\,\mathrm{Hz}$, and for the phonons $\omega_A \approx 10^{9}\,\mathrm{Hz}$, in order to have more or less the same energy in both fields there would be 10^5 more phonons than photons, $N_L << N_A$ so it is possible to use the given field approximation for the acoustic field.

In every physical interaction there are some measurable properties that must be conserved, for this subject, these ones are the energy and the linear momentum. In quantum mechanics, the linear momentum of a particle is:

$$\mathbf{p} = \hbar\,\mathbf{k}, \tag{1.15}$$

where $\mathbf{k}$ is the wave vector. So the relations that must be satisfied are:

$$\mathbf{E_L} + \mathbf{E_A} = \mathbf{E_+} \tag{1.16a}$$

$$\vec{\mathbf{p}}_\mathbf{L} + \vec{\mathbf{p}}_\mathbf{A} = \vec{\mathbf{p}}_\mathbf{+} \tag{1.16b}$$

where $\mathbf{E}$ stands for energy, $\mathbf{p}$ for momentum, the subscripts $\mathbf{L}$ and $\mathbf{A}$ are for the light and the acoustic fields, and the subscripts $+$ is for the scattered light. Using Eq. (1.14), (1.15), (1.16a) and (1.16b) is possible to arrive to two conditions:

$$\omega_0 + \Omega = \omega_1, \tag{1.17a}$$

$$\vec{k}_0 + \vec{K} = \vec{k}_1, \tag{1.17b}$$

here the subscripts 0 and 1 are for the incident and the scattered light, from now on the uppercase greek letter Ω and uppercase $\mathbf{K}$ are for the acoustic frequency and the acoustic wave vector respectively. This conditions can be displayed in the so called "wave vector diagrams", see Fig. 1.7. In the diagrams each vector represents the wave vector of each interacting particle and the resultant vector is the scattered photon.

These diagrams will help to visualize the two kinds of scattering that will be studied: the normal and the anomalous scattering. In the normal case, the scattered light will continue on the same surface, see Fig. 1.7, and in the anomalous case, the scattered light will "jump" to other surface, see Fig. 1.8.

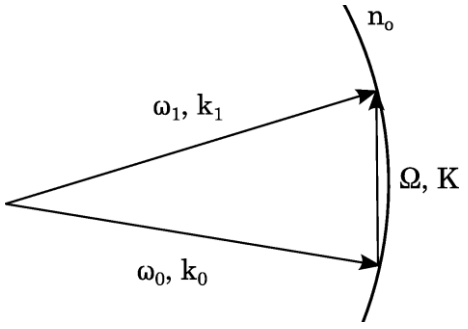

Figure 1.7 Simple wave vector diagram of light scattering in isotropic media.

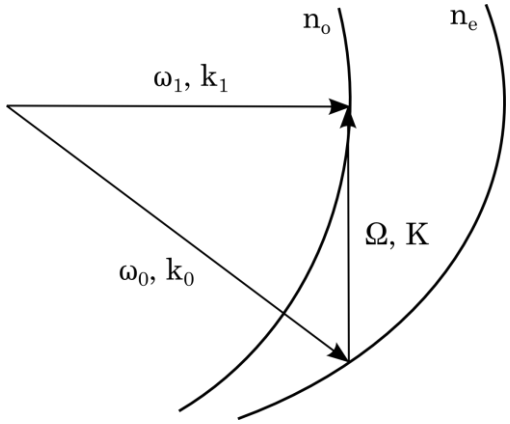

Figure 1.8 Anomalous light scattering in an anisotropic media.

Note that the anomalous light scattering cannot occur in isotropic media because there is just one surface. On the other hand, the normal light scattering can occur on both, isotropic and anisotropic media.

1.3.2. Collinear Interaction

This kind of interaction takes place when the acoustic wave and the optical wave are in the same direction. With the aid of the wave vectors is easy to see that collinear interaction is only possible on anisotropic media, see Fig. 1.9, nevertheless, this interaction has been reported to exist on isotropic media in a more complex phenomenon called "backward collinear acousto optic interaction" [1.3] but that matter is out of the interest of this thesis. In Fig. 1.9, is shown the collinear interaction on anisotropic media, where the photon absorbs one phonon to change its wave vector, in so doing the light will not change its direction but other properties such as polarization state. The basic arrangement for the collinear interaction will be depicted in chapter 3.

1.3.3. Non-Collinear Interaction

This is the most versatile interaction because it has more degrees of freedom. Here exist an angle between the optical wave and the acoustic wave directions, Fig. 1.8. In this interaction the light can stay in the same wave vector surface by changing its direction, it even can jump to another wave vector surface and then come back to the previous surface (two phonon light scattering), see Fig. 1.10. It can occur on both, isotropic and anisotropic media (Fig. 1.7 and 1.8),

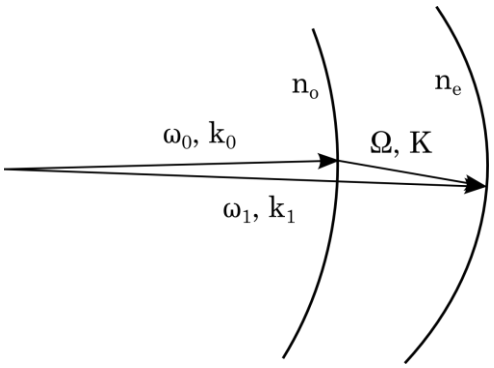

Figure 1.9 Cuasi-collinear interaction in an anisotropic media, in the collinear interaction the three wave vectors are in the same line.

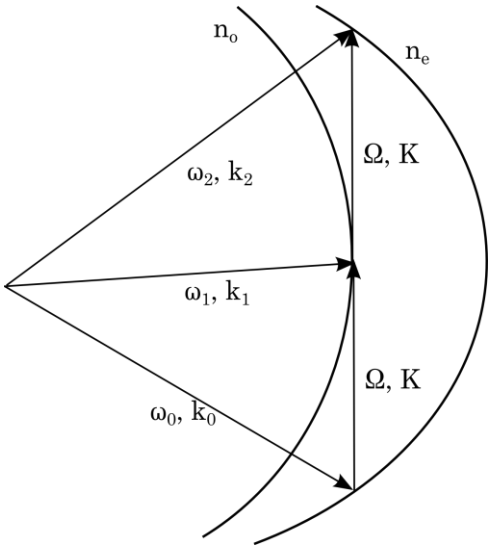

Figure 1.10 Two-phonon light scattering occurred in anisotropic media.

1.4. The Formal Approach (Differential Equation Method)

This method starts with the Maxwell's equations for a dielectric medium with a changing dielectric constant $\varepsilon(x,y,t)$ as a function of position and time. After some well known operations, the Maxwell's equations give the differential equation for the electric field of light as

$$\nabla^2 E - \frac{1}{c^2}\frac{\partial^2}{\partial t^2}(\varepsilon E) = 0 \tag{1.18}$$

Now the particular interaction geometry illustrated in Fig. 1.11 is considered. In this geometry the acoustic wave propagates in the x direction with and angles $\pm\varphi$, where

$$\varphi = \frac{\Lambda}{2L} \ , \tag{1.19}$$

and Λ is the wavelenght of the acoustic wave, the acoustic wave has an infinite depth in the y direction, and the width of the acoustic wave extends from $-L/2$ to $L/2$ in the z direction. The geometry assumes that a monocromatic plane wave of light is incident from the left downward on the sound column at and angle θ from the z axis. This geometry eliminates the $y-$axis dependence of the problem. The time and spatial dependence of the dielectric constant due to the presence of the acoustic wave can be written in the form

$$\varepsilon = \varepsilon_0 + \delta\varepsilon \sin(Kx - \Omega t) \tag{1.20}$$

K is the wave vector of the acoustic wave, Ω is the angular frequency of the acoustic wave. Although ε is a tensor quantity, it is assumed, for simplicity,

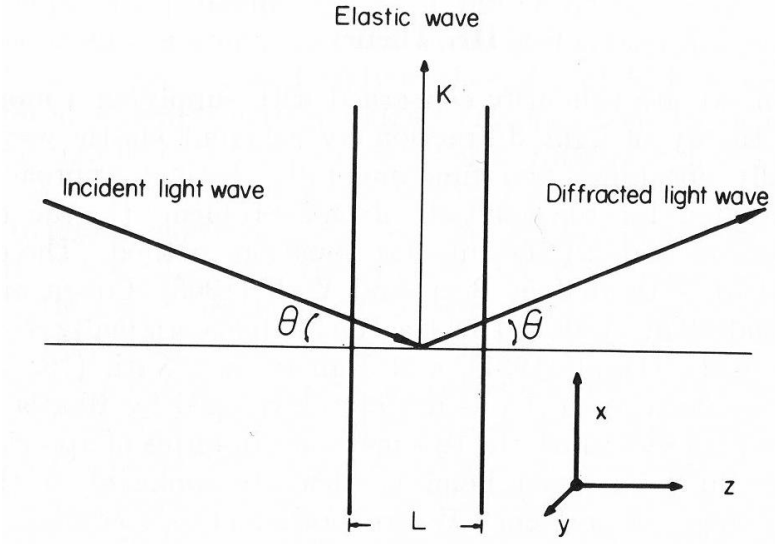

Figure 1.11 Geometry oy the acousto-optic interaction in a medium of leght L, an acoustic wave K and incident light at an angle θ.

that it can be represented by a scalar. With this geometry the electric field can be written in the form

$$E = U_0 \exp[i(kx\sin\theta - kz\cos\theta - \omega t)] \tag{1.21}$$

Now, it is possible to assume that the solution of the diffracted light is given by the sum

$$E = \sum_l U_l(z)\exp\{-i[(\omega + l\Omega)t - (k\sin\theta - lK)x + kz\cos\theta]\} \tag{1.22}$$

This sum represents a series in plane waves whose amplitudes $U_l(z)$ vary within the crystal along the z coordinate. Each plane wave, except U_0, originates from the absorption or emission of one or more phonons by the incident light beam in the interaction volume but this particular representation is only valid for $l = 1,2$.

This solution is substituted into Eq.(1.18). If the amplitude of each of the diffracted plane waves increases slowly with distance z z, the resulting terms in d^2U_l/dz^2 can be neglected. Also one can neglect the terms which are relatively small by the factor $\Omega/\omega << 1$ and the factor $V/c << 1$. Using the substitutions $k = \omega/c$ and $K = \Omega/V$, the resulting equations for the amplitude factors $U_l(z)$ are

$$U'_l(z) + i\beta_l U_l(z) - \xi[U_{l+1}(z) - U_{l-1}(z)] = 0 \tag{1.23}$$

where

$$\beta_l = -\frac{Kl}{\cos\theta}\left(\sin\theta + \frac{lK}{2k}\right), \qquad \xi_l = \frac{1}{4}\frac{\delta\varepsilon}{\varepsilon_0}\frac{k}{\cos\theta} \tag{1.24}$$

The general solution for the equations system in Eq.(1.23) is very complicated so it is considered that $U_{l+1} << U_l$ and that initially only $U_0 \neq 0$. The equation for U_l can be written as

$$\frac{\partial U_l}{\partial z} + i\beta U_l = -\xi U_{l-1} \tag{1.25}$$

The solution for this differential equation can be written in the form

$$U_l = -\exp(-i\beta_l z)\int_{-\infty}^{z} \xi U_{l-1}\exp(i\beta_l z')\,dz' \tag{1.26}$$

Now the case $l = 1$ is considered, it corresponds to the first order diffraction. If the acoustic-wave amplitude is uniform and nonzero only in the range $-L/2$ to $L/2$, then ξ is constant and nonzero only within the same limits. And, since $U_1 << U_0$, it is assumed that the diffraction process removes a negligible fraction of the incident light beam power. Thus, U_0 is basically constant in value and the amplitude of the first order diffracted light is

$$U_l = -\exp(-i\beta_1 z)\,\xi U_0\int_{-L/2}^{L/2}\exp(i\beta_1 z')\,dz'$$

$$U_l = \exp(-i\beta_1 z)\,\xi U_0 L \frac{\sin(\beta_1 L/2)}{\beta_1 L/2} \tag{1.27}$$

where

$$\beta_1 = -\frac{K}{\cos\theta}\left(\sin\theta + \frac{K}{2k}\right) \tag{1.28}$$

Using Eq.(1.23) is possible to estimate the fractional amount of light intensity which is diffracted by the acoustic wave as

$$\frac{I_1}{I_0} = \frac{U_1 U_1^*}{U_0 U_0^*} = \xi_1^2 L^2 \frac{\sin^2(\beta_1 L/2)}{(\beta_1 L/2)^2} \tag{1.29}$$

The maximum amount of power diffracted into one order occurs when $\beta_1 = 0$. For this condition,

$$\frac{I_1(max)}{I_0} = (\xi_1 L)^2 \tag{1.30}$$

Second order diffraction occurs when the light beam is scattered by two phonons. Using Eq. (1.21) and solving the equation system while assuming that $U_{l+1} << U_l$ and $U_0 \neq 0$, is possible to find the amplitude for the second order diffraction. This gives

$$\frac{d^2U_2}{dz^2} + 2i\beta_1 \frac{dU_2}{dz} - \beta_1\beta_2 U_2 = \xi^2 U_0 \tag{1.31}$$

Neglecting the first term and assuming that the amplitude of the acoustic wave is uniform and nonzero between $-L/2$ to $L/2$ gives the result

$$U_2 = \frac{\xi^2 L U_0}{2i\beta_1}\exp\left(-\frac{i\beta_2 z}{2}\right)\frac{\sin(\beta_2 L/4)}{\beta_2 L/4} \tag{1.32}$$

The use of Bragg diffraction is based on the results obtained in Eqs.(1.26) which express the diffracted light amplitude in terms of the scattering parameters and the experimental conditions. Using the particular case of an optical beam passing through a uniform-intensity acoustic beam of width L, the diffracted light amplitude for the second order is Eq. (1.32). where, using Eq. (1.24)

$$\beta_2 = -\frac{2K\left(\sin\theta + \frac{K}{k}\right)}{\cos\theta}$$

$$\xi_2 = \frac{1}{4}\frac{\delta\varepsilon}{\varepsilon_0}\frac{k}{\cos\theta}$$

The central maximum of the diffraction pattern occurs when $\beta_2 = 0$, which leads to

$$\frac{K}{k} = \sin\theta \tag{1.33}$$

where $\frac{K}{k}=\frac{\lambda f_c}{V}$, V is the speed of the acoustic wave, f_c is the central frequency of the scattered light and λ is the wavelength inside the material. The relative peak intensity of the diffracted beam is

$$U_2=\frac{\xi^2 L U_0}{2\beta_1}. \tag{1.34}$$

By differentiating Eq. (1.33), one obtains the diffraction bandwidth

$$\Delta f=\frac{2V}{\lambda}(\cos\theta)\frac{\Lambda}{L} \tag{1.35}$$

1.5. Applications of Modulation, Filtering and Deflection

There are several applications for acousto-optics and each one can reach different limits according to the materials and techniques used. Here is presented a brief explanation of the three applications which will be exploited in this thesis.

Light Modulation

This application consist in the modulation of light intensity of one selected diffraction order, usually the first order, while blocking the rest of the orders. The modulation of the selected order is achieved by increasing the diffraction efficiency given by

$$\eta=\frac{I_1}{I_{in}}=\sin^2\left(\frac{\pi}{2}\frac{P_a}{P_{peak}}\right)^{1/2}, \tag{1.36}$$

defined as the ratio of the power of the first order divided by the incident light power, P_a is the acoustic beam power and P_{peak} is the power of the peak diffraction efficiency.

For the zeroth-order, the diffraction efficiency can be approximated by the complement of the first-order diffraction efficiency;

$$\eta=\frac{I_0}{I_{in}}=\cos^2\left(\frac{\pi}{2}\frac{P_a}{P_{peak}}\right)^{1/2}. \tag{1.37}$$

The major performance is given by the response time related to the transit time τ defined as the time required for the acoustic beam to travels through the light beam,

$$\tau=\frac{D_{in}}{V_s}, \tag{1.38}$$

where D_{in} is the diameter of the light beam and V_s is the velocity of the sound in the media.

Deflection

It is used for very precise deflection of light beams, the acousto-optic (AO) deflector designed to diffracts a collimated light beam into a single order whose spatial position will be determined by the frequency of the acoustic wave applied to the device. When working in the Bragg regime, it is called Bragg cell. Using the conservation of momentum is possible to estimate the angle of deflection,

$$\vec{k}_d = \vec{k}_i + \vec{K} \tag{1.39}$$

where $\vec{k}_d$ is the wave vector of the deflected light, $\vec{k}_i$ for the incident light and $\vec{K}$ for the acoustic wave, which magnitude is:

$$K = 2k \sin\theta_B , \tag{1.40a}$$

$$\theta_B = \sin^{-1} \frac{\lambda_0}{2n\Lambda} , \tag{1.40b}$$

here n is the index of refraction of the AO medium, λ_0 is the free-space wavelength of the light, and Λ is the acoustic wavelength. θ_B is called the Bragg angle, note that this is the same angle that maximizes the amount of light diffracted in Eq. (1.29). When the AO cell is illuminated at this angle, the total angle of deflection is

$$\theta_D = 2\theta_B \approx \frac{\lambda_0 f}{nV} \tag{1.41}$$

where f is the frequency of the acoustic wave, so the angle of deflection is proportional to this frequency.

Filtering

Generally, there exist two kinds of AO filters: isotropic AO filters, which use a pinhole for selectivity, and collinear filters made with anisotropic crystals. The second kind is more common and this work will focus on that type of filters. The condition for such an interaction to exist is

$$f = \frac{\Delta n\, V}{\lambda_v} , \tag{1.42}$$

where $\Delta n = n_e - n_o$ and λ_v is the wavelength of the light in the crystal. The resolution can be estimated as

$$\delta f = \frac{1}{\tau} = \frac{V}{L} , \tag{1.43}$$

where τ is the sound transit time and L the collinear interaction length. Based on this, longer interaction lengths help to improve the frequency resolution

For optically anisotropic media, the acousto-optical interaction can change the polarization state of the light, see Fig. 1.8 and 1.9. This can be exploited to filter the scattered from the non-scattered light using an acousto-optical cell between crossed polarizers and will be explained in more details in chapter 3.

1.6. Acousto-Optic properties of Materials

The most important characteristics concerned for the acousto-optical interaction are listed and their values for some selected materials are shown in Table 1.1. When choosing a material to work with, there are several aspects one look forward, and depending on the selected application, the material could develop great in some aspect but very bad in other ones. There is no perfect material and it is necessary to find a balance in its properties to have the best overall performance, for example; TeO_2 has a very large figure of merit M_2, which is a good quality, but its high acoustic losses set a limit for its use in some applications.

Range of transmission

One of the most important thing to take into account is the range of transmission. This parameter tell us which light wavelengths are not (or less) absorbed by the material. Some crystal could have the best acoustic properties for some specific problem but will be useless if all the light is absorbed or even reflected.

Sound velocity

This parameter can be estimated using considering a simple model of an array of points of mass M separated a distance a and bounded by springs of constant C. By taking into account just the nearest neighbor interactions the sound velocity is [1.4]

$$V = \sqrt{\frac{Ca^2}{M}} \tag{1.44}$$

Measured in cm/s, this characteristic is closely related with the figure of merit, which is described later, but also have an important role for generating the index gratings. As it is known,

$$\Lambda = \frac{V}{\Omega}, \tag{1.45}$$

where V is the velocity of the sound, Ω is the frequency injected by the piezoelectric transducer, and Λ is the wavelength of the sound, which will be directly related to the period of the grating. With this in mind, with a small velocity will be easier to generate gratings with more lines per centimeter because not too high frequencies on the piezoelectric will be needed.

Acoustic losses

For the study of this characteristic an important parameter is the ratio of the acoustic wavelength Ω and the mean free path of phonons. The mean free path, in turn, is the inverse of τ, the collision time between phonons. If $\Omega\tau >> 1$ the acoustic losses will come from the lattice phonons in thermal equilibrium. The other regime, when $\Omega\tau << 1$, is more interesting for this work. Here the mean free path of thermal phonons is smaller than the acoustic wavelength. The higher density regions will have greater temperature than the lower density regions and this will produce thermal

conduction between them, as a result, energy from the acoustic wave will be subtracted. The previous analysis is not enough to explain the experimentally observed acoustic losses so another mechanism should exist. The Akhiezer mechanism of sound absorption was formulated to treat this phenomenon described as a phonon viscosity effect.
The attenuation α per unit path length is [1.5]:

$$\alpha \approx A\frac{\Omega^2\tau_r}{V}, \tag{1.46}$$

where A is a constant to be determined, τ_r is the relaxation time of the thermal phonons. With this result one can say that the losses are proportional to the acoustic frequency and that low-velocity materials have higher losses than the high-velocity materials.

Figures of Merit
The efficiency of the light diffracted at the Bragg angle is [1.6]:

$$\eta = \frac{I_1}{I_0} = \frac{\pi^2}{2}\left(\frac{P_a/LH}{\rho V^3}\right)\left(\frac{n^3 p_{eff} L}{\lambda_0 \cos\theta}\right)^2 \tag{1.47}$$

where $P_a = LHI$ is the acoustic power in a beam of intensity I with width L and height H. Smith and Korpel in 1965 [1.6] propose M_2 as a figure of merit for materials operating under the Bragg conditions:

$$M_2 = \frac{n^6 {p_{eff}}^2}{\rho V^3}, \tag{1.48}$$

where n is the refractive index, ρ is the density of the material, p_{eff} is the effective photo-elastic constant, and V is the acoustic velocity.
The efficiency is proportional to the acoustic beam width but the bandwidth, according to Eq. (1.35), is inversely proportional to the beam width. In 1966, Gordon [1.7] proposed a quantity independent of the width,

$$2\eta f_0 \Delta f = \left(\frac{n^7 {p_{eff}}^2}{\rho V}\right)\frac{2\pi^2}{{\lambda_0}^3 \cos\theta}\frac{P_a}{H}. \tag{1.49}$$

The factor

$$M_1 = \left(\frac{n^7 {p_{eff}}^2}{\rho V}\right) \tag{1.50}$$

is another figure of merit for materials used in modulators and deflectors.
In Eq.(1.47) and Eq.(1.49) it was assumed that the acoustic beam height is larger than the light beam diameter. Reducing the acoustic beam height to the size of the light beam and using the relation $\Lambda/L = \lambda/\varpi$ to have tho same spreading angles in both optical and acoustic beams, one can get the quantity [1.8]

$$f_0\eta = \left(\frac{n^7 p_{eff}^2}{\rho V^2}\right)\frac{\mu^2}{\lambda_0^3 \cos\theta}P_a \tag{1.51}$$

which is, in contrast with Eq.(1.47) and Eq.(1.49), independent of the sizes of the acoustic and optical beams. With this, it is possible to set

$$M_3 = \left(\frac{n^7 p_{eff}^2}{\rho V^2}\right), \tag{1.52}$$

as the third figure of merit. Each figure of merit will have certain relevance depending on the conditions of the acoustic-optical cell. For the interest of this work, the most relevant will be the figure of merit M_2.

Elasto-optic Tensor

Also knowing as strain-optic tensor, is a physical quantity which relates the strain tensor and the index of refraction through the acousto-optical interaction. This interaction occurs in all states of matter and is described by

$$\Delta\eta_{ij} = \Delta\left(\frac{1}{n^2}\right)_{ij} = p_{ijkl}u_{kl} \tag{1.53}$$

where $\Delta\eta_{ij}$ is the change in the optical impermeability tensor, u_{ij} is the strain tensor, and p_{ijkl} is the elasto-optic tensor. An acoustic wave in a crystal change the index ellipsoid of the crystal Eq. (1.1) to

$$(\eta_{ij} + p_{ijkl}u_{kl})\, x_i x_j = 1. \tag{1.54}$$

Due to the symmetry of the strain and the impermeability tensor, the indices i and j as well as k and l can be permuted. The elasto-optic tensor has the same symmetry of the quadratic electro-optic tensor [Yariv] so one can use the contracted indices to simplify Eq. (1.53) to

$$\Delta\left(\frac{1}{n^2}\right)_{ij} = p_{ij}u_j. \tag{1.55}$$

Photo-elastic constant

This constant can be estimated using the photo-elastic tensor p_{ijkl}, the strain tensor u_{kl}, the direction of the sound wave in the crystal $\vec{d}_1$, and the direction of the interacting light $\vec{d}_0$. The effective photo-elastic constant is

$$p_{eff} = \vec{d}_1\, p_{ijkl} u_{kl}\, \vec{d}_0, \qquad i,j = 1,2,\ldots,6, \tag{1.56}$$

and using the Eqs. (1.53) and (1.54) one can rewrite Eq. (1.56) with the contracted indices to simplify the notation. Equation (1.56) then becomes

$$p_{eff} = \vec{d}_1\, p_{ij} u_j\, \vec{d}_0 \tag{1.57}$$

Table 1.1 List of acousto-optical materials with their principal characteristics in their most used mode.

Material	Symmetry	Range of transm. **[μm]**	**λ [μm]**	**V [10^5 cm/s]**	Mode & prop. dir.	**Γ** $\left[\frac{dB}{cm\ GHz^2}\right]$	**M_2** $\left[10^{-18}\frac{s^3}{g}\right]$	**n**
SiO_2	32	.12 – 4.5	0.589	6.32	L[001]	2.1	1.48	1.54
TeO_2	422	0.35 – 5	0.633	0.62	S[110]	288.7	1200	2.26
$CaMoO_4$	4/m	0.45 – 3.8	0.671	2.95	S[100]	60	1.98	1.98
H_2O	Isotropic	0.2 – 0.9	0.633	1.49	L	2400	126	1.33
KRS – 5	m3m	0.58 – 32	0.671	1.92	L[111]	10	930	2.57
Hg_2Cl_2	4/mmm	0.38 – 28	0.633	0.347	S[110]	230.5	703	2.27
$Bi_{12}GeO_{20}$	23	0.45 – 7.5	0.633	1.77	S[110]	2.5	5.17	2.55
$Bi_{12}SiO_{20}$	23	0.45 – 7.5	0.633	3.83	L[100]	2.5	9.02	2.55
$LiNbO_3$	3m	0.4 – 5	0.633	6.57	L[100]	0.15*	7.0	2.20

1.7. Formulation of Problems

A new acousto-optical dynamic diffraction grating for the spectrometer
The Guillermo Haro astrophysical observatory uses an optical spectrometer with several exchangeable traditional (made of a suitable optical glass i.e. static in behavior) diffraction gratings as the dispersive elements. Due to the current needs of astrophysical observations the resolution of spectrometer has to be changed time to time that can be done only by mechanical substitution of one static diffraction grating with another one. Every time the static grating is substituted, the spectrometer needs to be realigned and recalibrated; however, it leads to potential errors in measurements and losing very important physically and rather expensive time for the observations. In order to improve this situation, an alternative for the static diffraction gratings has been proposed: to use specially designed acousto-optical cell as the dynamic (i.e. completely electronically tunable) diffraction grating, whose capabilities will make it possible in the nearest future to replace all the static diffraction gratings from the spectrometer. The principal advantages of similar dynamic acousto-optical grating are excluding any mechanical operations within the observation process, avoiding recalibrations (i.e. bringing in additional errors) and any losses of time. In connection with this, the first steps in design of a desirable acousto-optical cell, adequate to the above-mentioned needs, are considered as the first problem within this thesis.

Acousto-optical filter
Usually, the performances of acousto-optical filters, exploited in linear regime and operated by low-level external electronic signals, are completely determined by the properties and size of a crystalline material chosen for the device. Nevertheless, preliminary and more detailed consideration of the filtering process makes it possible to predict that a specific mechanism of the acousto-optic nonlinearity capable to regulate performances of the collinear acousto-optical filter exist and could be used practically. That is why the possibility of analyze this mechanism theoretically and try to confirm it experimentally with an advanced filter based on calcium molybdate ($CaMoO_4$) single-crystal and governed by external signals of finite amplitude is formulated as the second problem within this thesis.

Triple Product Processor
Detailed studies in the extra-galactic astronomy and searching the extra-solar planets are now actual avenues of astrophysical investigations. One of the most powerful instruments in both these areas is the precise multi-channel spectrum analysis of radio-wave signals. Recently performed estimations show that the algorithm of space-and-time integrating could be definitely suitable for a wideband spectrum analysis with an ultimate frequency resolution. This algorithm requires an advanced acousto-optical processor to produce the folded spectrum of those signals, accumulating advantages of space and time integrating. In a view of similar requirement, developing a schematic arrangement for the triple product acousto-optical processor based on at least 3-inch optical components of a top-level quality is suggested as the third problem for this thesis.

Chapter 2

Acousto-Optical Version of Optical Spectrometer for Guillermo Haro Observatory

Optical spectrometer of the Guillermo Haro astrophysical observatory (Mexico) exploits mechanically removable traditional static diffraction gratings as dispersive elements. There is a set of the static gratings with the slit-density **50 – 600 lines/mm** and optical apertures **9 cm x 9 cm** that provide the first order spectral resolution from **9.6** to **0.8 A/pixel**, respectively, in the range **400 – 1000 nm**. However, the needed mechanical manipulations, namely, replacing the static diffraction gratings with various resolutions and following recalibration of spectrometer within studying even the same object are inconvenient and lead to losing rather expensive observation time. Exploiting an acousto-optical cell is suggested, i.e. the dynamic diffraction grating tunable electronically, as dispersive element in that spectrometer.which can realize tuning both the spectral resolution and the range of observation electronically and exclude filters.

2.1. Introduction

The Boller & Chivens (B & C) Cassegrain spectrographs available at Guillermo Haro Observatory (GHO) are classical grating spectrographs. Presently, B & C spectrograph is available on GHO at the 2.12m telescope with 9 gratings, allowing a good coverage in both dispersion and wavelength within the CCD sensitivity ranges. The observer can communicate most of the commands necessary to control the spectrographs through a display console in the control room.

The B & C spectrograph design is shown in Fig. 2.1. The converging light beam from the telescope passes through the spectrograph entrance slit in the telescope focal plane to the collimator, an off-axis parabolic mirror. The reflected parallel beam then falls on to the grating surface. The diffracted

light passes through a Schmidt camera which images the spectrum on to the CCD detector. The slit assemblies consist of two 64mm long polished and aluminized jaws on which the stellar image can be seen by reflection. The slit jaws form a biparting slit that is continuously adjustable by a micrometer screw from 50 to 1200 μm. Note that the slit appears smaller to the detector than is the real width (called projected slit-width). This is due to two effects. Firstly, because of the transversal magnification factor", and secondly, to the grating anamorphism. The apparent reduction in slit-width can be compensated for by selecting the required resolution at the detector and calculating back the slit-width. For example, if a projected slit width on the CCD detector of 30 μm is required (2 x *15* μm pixels), then the real slit-width should be 30/(0.78 x δ (= 0.191)) = *201*μm. Here, it is assumed that the spectrometer is working at a grating angle of *15°.*

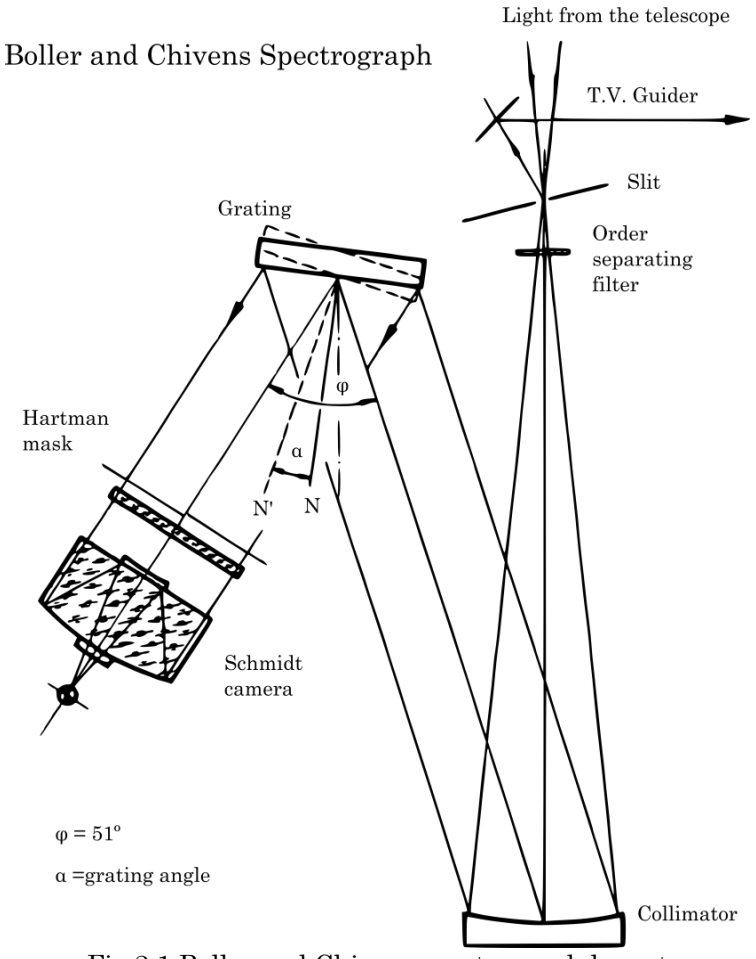

Fig 2.1 Boller and Chivens spectrograph layout

The opto-mechanical configuration allows for a fixed angle between the incident and diffracted beam axis of the grating (grating angle α). The grating is mounted in an adjustable rotating cell that permits the choice of the central wavelength and spectral orders.

The spectrograph cameras currently in use at the 2.12 m telescopes have a focal length of 465 mm and are optimized for use over the range 3200-

12000 Å where they have an efficiency of about 50 - 55 %. Below 3200 Å , the efficiency drops rapidly to 10% at 3000 Å . A field-flattening lens is also mounted immediately in front of the CCD dewar in order to correct for camera field curvature.

An order blocking filter assembly is located below the slit jaws to prevent overlapping of unwanted spectral orders. The 2.12m spectrograph may hold up to four filters. The correct choice of filter is normally determined by the optical group and installed before an observing run. No deckers are used with the B & C spectrographs for observation. There is a decker mounted in front of the slit, but this is used for setup purposes only.

Detectors

The CCD detector of the Boller & Chivens spectrograph is a back illuminated Tektronix chip of format 1024x1024 pixels (TK1024AB grade 1)

Calibration Lamps

Calibration lamps are mounted at 2.12m, one blue halogen lamp for flat-fielding and one Helium-Argon spectral lamp for wavelength calibration. Lamp selection and illumination is done remotely. A neutral density wheel is also available at the 2.12m. These can be used to attenuate both the He-Ar and the internal flat-field lamps.

Instrumental Rotation

The Cassegrain adapters on telescope can be rotated up to 180º in either direction. For the 2.12m telescope, the rotation has to be done manually in the dome. This Cassegrain adapters have scales for accurately setting the position angles of the spectrograph slit. Instrument rotation can be done with the 3.6m telescope at any zenith distance. However, since the rotation at the 2.12m telescope is done manually, this is usually done with the telescope at the zenith to facilitate reading of the position angle scale on the Cassegrain adaptor. This is particularly important for the 2.12m telescopes, since, once the spectrograph is unclamped ready for rotation, it may start to rotate rapidly as the spectrograph is not balanced about the optical axis.

TV Acquisition and Guiding

The front surfaces of the spectrograph slits are aluminized and tilted slightly with respect to the incoming beam to allow the use of an integrating TV acquisition and guiding system. There is also a "field-viewing" position (approximate field, 5' x 4') for object acquisition. A visual magnitude (V) ~ 20 mag star can be seen without integration on a moonless night on the center field camera. The 2.12m telescope also has an intensified camera for auto guiding. Under good moonless conditions stars of V ~ 18 can be seen. Note that these are approximate magnitudes and critically depend on focusing, seeing etc.

2.2. Guillermo Haro Observatory Spectrograph Performances

Available Gratings

The Observatory has 9 gratings available. All gratings are 90 x 90 mm and are used mostly in the first and second order with dispersions ranging from 29 to 450 Å mm^{-1}.

For some gratings, the astronomer must consider the different efficiencies encountered for the polarization directions both parallel and normal to the grooves, especially for highly polarized objects. For most astronomical observations, however, the average between the two polarization efficiencies is sufficiently accurate.

Spectral Coverage

The grating dispersion, camera focal length, and detector size determine the observable spectral range. For example, grating # 21, which has a dispersion of 172 Å mm^{-1}, when used in the first order will provide a spectral coverage of 172 X 15.36 = 2642 Å with a high resolution RCA chip (1024 X 15 μm = 15.36 mm). Given that the grating is centered at λ 5400 Å, the wavelength limits will be 4079 Å and 6721 Å.

Spectral Resolution

The *theoretical* spectral resolution depends on the grating dispersion, grating position, pixel size, collimator and camera focal length, and entrance slit-width. The *effective* CCD spectral resolution also depends on the detector sampling. A detailed calculation of these parameters is shown later in this text.

As an example, a grating with blaze angle 6°54', centered for **5400 Å** will have *theoretical* resolutions of 1.72 and 3.45 Å for slit-widths of 1" and 2" respectively. Decreasing the entrance slit-width will improve the resolution. However, this will be possible only when the sampling requirements (Nyquist criterion; one resolution element imaged onto at least two detector elements) are respected and also when the instrumental response is not diffraction limited.

Spatial Resolution

The spatial resolution depends on the transversal magnification factor of the spectrograph given in Table 2.1. (This spatial scale can easily be determined by moving a star a known distance along the slit and taking an exposure at both positions.

The CCD control program allows the CCD pixels to be binned in either direction (spatial or dispersion) before reading out. This can be an advantage when the objects are faint in which case may be wanted to bin in the spatial direction. No spectral resolution will be lost but there will be a decrease in the read-out-noise by a factor of the square root of the number of pixels binned. Therefore, this may allow the use of shorter exposure times and higher signal-to-noise ratios at the cost of decreased spatial and/or spectral

resolutions, depending on which direction you are binning. Also, binning increases the risk of cosmic ray events influencing data since several pixels are averaged before readout. Furthermore, binning also reduces the contrast of particle events making automatic removal more difficult. Should spectral resolution be of vital importance, bin the chip only along the X (spatial) direction.

The CCD program also allows "readout windowing". This means that only those pixels within a predefined window or area on the chip are recorded. The spectrograph slits do not extend across the entire width of the CCDs and therefore no information is contained outside the length of the slit. Windowing can thus provide significant savings in the sizes of your data files and image display time.

Grating Efficiencies

The efficiency as well as the dispersion at the desired working wavelength is an important parameter when choosing a grating. The efficiencies of the available gratings have been measured experimentally one is shown in Fig. (2.2). Note that the *total* system efficiency is the combination of the efficiencies of the telescope, spectrograph, grating, camera and the detector.

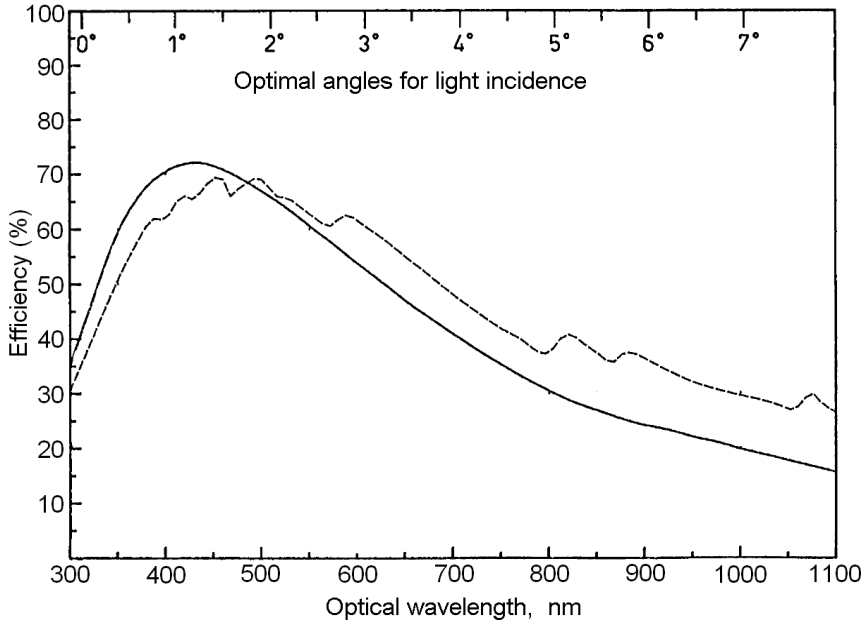

Figure 2.2. Maximum diffraction (reflection) efficiency of the static diffraction grating with: the slit-density **300 lines/mm**, dispersion **224 Å mm^{-1}** , and blaze angle of **$\theta = 4°18'$** : solid line is for the light polarized parallel to slits and dashed line is for the light polarized perpendicular to slits.

Total efficiency

The total telescope efficiency is the ratio of the number of detected photons divided by the number of incident photons entering the telescope. This latter quantity is found for standard stars from:

$$N_\lambda = L \times \frac{4.5 \times 10^{10}}{\lambda} \times 10^{-0.4(m_v + A_\lambda x)} \qquad (2.1)$$

where, L is the telescope primary mirror area in square meters and N_λ. is the number of photons at wavelength λ incident on the telescope per second and Angstrom. A_λ. is the mean extinction coefficient and x is the airmass. The values of m_v are found from tables of standard stars.

Expected S/N ratios
The *expected S/N* ratio obtained by a CCD with a finite read-out-noise and dark current, is:

$$\frac{S}{N} = \frac{3600 n_0 t \times 10^{-0.4(m-m_0)}}{[3600 n_0 t \times 10^{-0.4(m-m_0)} + (\omega b^{-1} N_r)^2 + \omega^2 tD]^{0.5}} \quad (2.2)$$

where n_0 is the efficiency in $e^{-1}s^{-1}pixel^{-1}$ for a star of magnitude m_0, ω is the width of the spectrum in pixels, perpendicular to dispersion, N_r is the read-out-noise in $e^{-1}\,pixel^{-1}$, D is dark current in $e^{-1}\,pixel^{-1}\,hr^{-1}$, t is the exposure time in hours, b is the binning factor perpendicular to the dispersion direction, and m is the stellar magnitude.

2.2.1. Calculations for the Spectral Resolutions

Here, it is presented the formulae for deriving the spectral resolution.

$$\theta = \sin^{-1}\left(\frac{nm\lambda}{2\times 10^7 \cos(\phi/2)}\right) \quad (2.3)$$

$$\omega' = \omega\left(\frac{f_2}{f_1}\right)\left(\frac{\cos(\theta+\phi/2)}{\cos(\theta-\phi/2)}\right) \quad (2.4)$$

$$D = \left(\frac{10^7 \cos(\theta-\phi/2)}{nmf_2}\right) \quad (2.5)$$

$$R_s = D\omega' = \left(\frac{10^4 \omega \cos(\theta+\phi/2)}{nmf_1}\right) \quad (2.6)$$

where λ is the central wavelength in Å, n is the number of lines per mm, m is the diffraction order, ϕ is the grating configuration angle (see Fig. 2.3), θ is the grating angle, ω is the entrance slit-width in μm, ω' is the projected slit-width in μm, f_1 is the collimator focal length in mm, f_2 is the camera focal length in mm, D is the dispersion in $Å\,mm^{-1}$, R_s is the theoretical spectrograph resolution in Å (without detector), and $\gamma = f_2/f_1$ is the transversal magnification factor

The effective CCD.spectral resolution is the convolution of R_s with the detector pixel size. With suitable detector sizes, the spectrum may be sufficiently sampled to avoid spectral information distortion (eg. line profile distortions). The common sampling criterion is $R_s = 2 pixels$ (i.e. Nyquist criterion).

2.3. Acousto-Optical Cell

In this chapter the potential use of an acousto-optical cell as a diffraction grating is discussed. In order to apply this for the design of the spectrograph, the parameters of the diffraction gratings, currently used, must be know, also its performance. Later, the analysis of the performance of the acousto-optic phase grating needs to be made to compare it with the previous gratings.

2.3.1. The nature of Acousto-optical dynamic diffraction grating

Photo-elastic effect consists in connection between the mechanical deformations γ or stresses σ and the optical refraction index $\mathbf{n}$. This effect takes place for all the condensed matters and mathematically can be explained as [2.1]

$$\Delta\zeta_{ij} = \Delta\left(\frac{1}{n^2}\right)_{ij} = p_{ijkl}\,\gamma_{kl} = \pi_{ijkl}\,\sigma_{kl}\ , \tag{2.7}$$

where $\Delta\zeta_{ij} = \Delta(1/n^2)_{ij}$ represents varying the tensor of optical impermeability or, what is the same, the parameters for an ellipsoid of optical refractive indices; while $\mathbf{p}$ and π are the tensors of photo-elastic and piezo-optical coefficients, respectively. Usually, the higher-order terms relative to the deformations γ or the stresses σ are omitted due to smallness about 10^{-5} of both the deformations γ and/or the stresses σ. The symmetry inherent in a medium determines non-zero factors of the tensors $\mathbf{p}$ and π. With non-zero external mechanical perturbations, an ellipsoid for the refractive indices can be explained by

$$\sum_{i,j}\left[\left(\frac{1}{n^2}\right)_{ij} + \Delta\left(\frac{1}{n^2}\right)_{ij}\right] x_i\,x_j = 1\ , \tag{2.8}$$

Due to all the tensors $\Delta\zeta$, $\mathbf{p}$, and π are symmetrical in behavior, one can use so-called matrix indices [2.1]. Now, let us consider propagation of the traveling harmonic longitudinal elastic wave along the $\vec{z}\,\|\,[001]$-axes through an isotropic medium, so that the displacement $\mathbf{u}$ of particles is described by $u_3(x_3,t) = U\cos(\Omega t - K x_3)$, where $\mathbf{U}$,Ω, and $\mathbf{K}$ are the amplitude, cyclic frequency, and wave number of that traveling elastic wave, respectively. The field of linear deformations $\gamma_{ij} = (1/2)\cdot[(\partial u_i/\partial x_j) + (\partial u_j/\partial x_i)]$, occurred by this wave, is $\gamma_{33} = K U \sin(\Omega t - K x_3)$. The components of the optical impermeability tensor can be written as

a) $\Delta\zeta_{11} = \Delta\zeta_{22} = p_{12} K U \sin(\Omega t - K x_3)$, b) $\Delta\zeta_{33} = p_{11} K U \sin(\Omega t - K x_3)$, 2.9)

while $\Delta\zeta_{ij} = 0$ for the indices $i \neq j$. Here, p_{mn} are the components of the photo-elastic tensor $\mathbf{p}$ with matrix indices. In this case, Eq.(2.8) gives

$$\left[\left(\frac{1}{n^2}\right)+p_{12}\,K\,U\sin(\Omega t-K x_3)\right]x_1^2+\left[\left(\frac{1}{n^2}\right)+p_{12}\,K\,U\sin(\Omega t-K x_3)\right]x_2^2+$$
$$\left[\left(\frac{1}{n^2}\right)+p_{11}\,K\,U\sin(\Omega t-K x_3)\right]x_3^2=1\ . \qquad (2.10)$$

Due to Eq.(2.10) does not include any cross-terms, the main axes inherent in a new ellipsoid for the refractive indices will have the same directions as before. Consequently, new main values N_j of the refractive indices can explained as

$$\text{a)}\ N_1=N_2=n-\frac{1}{2}n^3p_{12}\,K\,U\sin(\Omega t-K x_3),$$
$$\text{b)}\ N_3=n-\frac{1}{2}n^3p_{11}\,K\,U\sin(\Omega t-K x_3). \qquad (2.11)$$

These equations mean that in the presence of the traveling acoustic wave, the taken isotropic medium becomes a periodic structure, which is equivalent to a bulk grating with the grating constant equal to the acoustic wavelength $2\pi/K=\Lambda$, because variations in the main refractive indices $\Delta n_{1,2}=n^3p_{12}\gamma_{33}$ and $\Delta n_3=n^3p_{11}\gamma_{33}$ are proportional to the amplitudes of displacement or/and deformations in that acoustic wave. An example for a sinusoidal variation of the refractive index is illustrated in Fig.2.3. This periodic perturbation in a medium is varying in space and in time as well. It represents a traveling wave propagating with the ultrasound velocity $V=\Omega/K$, whose magnitude in the condensed matters is typically equal to about $(1-7)\cdot10^5$ cm/s. However, the light velocity exceeds this magnitude by about 5 orders, so that periodic perturbations conditioned by that acoustic wave can be always considered as quasi-static in behavior relative to light propagation. Thus, potential resolution R of similar diffraction grating measured in the number of slits per unit aperture d (let us say, for $d=1$ mm) or, what is the same, the line density can be determined by the ratio $R=d/\Lambda$.

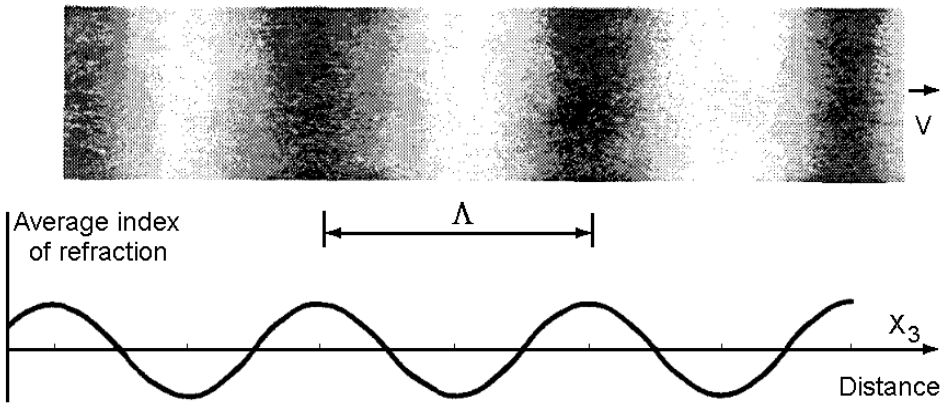

Figure 2.3. The instantly frozen acoustic wave, which consists of alternating with one another areas of compressed and decompressed material density and the corresponding sinusoidal variations of the refractive index.

2.3.2.Requirements and Design

The list of the, currently in use, diffraction gratings is shown in Table 2.1.

Table 2.1 List of static diffraction gratings available at the GHO with their specific wavelength of operation and resolution.

lines/mm	Blaze wavelength (Å)	Resolution (Å/pixel)	Order
150	5000	3.2	1
300	5000	1.6	1
300	7500	1.6	1
600	7500	0.8	1
600	4850	0.8	1

2.3.3.Material Selection

The requirements to the acousto-optical cell (AOC) combine a large optical aperture with the needed slit-density $\mathbf{R}$, an acceptable level of uniformity for acoustical grooves limited by linear acoustical losses in the chosen material, and possibly high efficiency of operation under an acceptable applied acoustic power. The list of the, currently in use, static diffraction gratings was shown in Table 2.2. This is why initially one have restricted the problem by the given slit-density (for example, $\mathbf{R = 300\ lines/mm}$), which leads to the inequality $\Lambda = V/f \le 1/R \quad (\approx 0.33 \cdot 10^{-3}\ \mathbf{cm})$, where $f = \Omega/2\pi$, i.e. to the requirement

$$f \ge f_{low} = V R \quad [\mathbf{MHz}] \,. \tag{2.12}$$

The other requirement is connected with the uniformity of acoustical grooves is restricted by the acoustic attenuation, whose level $\mathbf{B}$ along the total optical aperture $\mathbf{D}$ of AOC should not exceed a given value, let say $\mathbf{6\,dB}$. The acoustic attenuation is a square-law function of the carrier acoustic frequency $\mathbf{f}$ [2.2]. Let us use the conventional factor Γ of acoustic attenuation [2.3] expressed in $\mathbf{dB/(cm \cdot GHz^2)}$. Thus various forms of limitations connected with acoustic attenuation can be written. For example, the total level $\mathbf{B\,[dB]}$ of acoustic attenuation can be expressed as

$$B\,[\mathrm{dB}] = \Gamma D f^2 = \Gamma D V^2 R^2 \,. \tag{2.13}$$

Table 2.2 demonstrates the carrier frequencies $\mathbf{f}$ allowing us to realize the AOC, which provide the slit-density $\mathbf{R = 300\ lines/mm}$ together with the potential total losses along the AOC aperture. Considering those values, one can find that the best performances are exhibited by the following pair of materials, namely, $\mathbf{Bi_{12}GeO_{20}}$ and $\mathbf{LiNbO_3}$, because of their very low acoustic losses. Nevertheless, even with acoustic losses $\mathbf{40}$ times larger, the figure of merit $\mathbf{M_2}$ of calomel ($\mathbf{Hg_2Cl_2}$)[2.3] is $\mathbf{100}$ times larger than the figure of merit of $\mathbf{Bi_{12}GeO_{20}}$, it is almost the same situation with the crystal $\mathbf{KRS-5}$. The rest of the materials cannot offer similar advantages so one must forget them.

Table 2.2. Estimations for the carrier frequencies $\mathbf{f}$ and the corresponding total acoustic losses $\mathbf{B\,[dB]}$ along the AOC with a $\mathbf{9\,cm}$-aperture for the dynamic grating with the slit-density of $\mathbf{R = 300\ lines/mm}$.

Material	$\mathbf{SiO_2}$	$\mathbf{TeO_2}$	$\mathbf{KRS-5}$	$\mathbf{Hg_2Cl_2}$	$\mathbf{Bi_{12}GeO_{20}}$	$\mathbf{Bi_{12}SiO_{20}}$	$\mathbf{LiNbO_3}$
$\mathbf{f}$ [GHz]	1.89	0.19	0.58	0.10	0.53	1.15	1.97
$\mathbf{B\,[dB]}$	68.0	89.9	29.9	22.51	6.3	29.7	5.2

Then, a given value of $\mathbf{B\,[dB]}$ for the acoustic attenuation will require the aperture of $\mathbf{D \le B\Gamma^{-1} f^{-2}}$ or the carrier frequency

$$\mathbf{f \le f_{up} = \sqrt{B/\Gamma D}\ \ [GHz]} \tag{2.14}$$

at a given optical aperture $\mathbf{D}$ within the chosen acousto-optical material. It is naturally to search for the materials allowing the choice of the carrier acoustic frequency $\mathbf{f}$ satisfying the combined inequality $\mathbf{f_{low} \le f \le f_{up}}$. Let us consider the case of $\mathbf{R = 300\ lines/mm}$, $\mathbf{D = 9\,cm}$, and $\mathbf{B = 6\,dB}$, which leads to the following choice [2.4, 2.5]:

1. $\mathbf{Bi_{12}GeO_{20}\ [110]}$, $\mathbf{V_{SS} = 1.77 \cdot 10^5\ cm/s}$, $\mathbf{\Gamma = 2.5\ dB/(cm \cdot GHz^2)}$: $\mathbf{f_{low} \approx 531\ MHz}$ and $\mathbf{f_{up} \approx 516\ MHz}$.

2. $\mathbf{LiNbO_3\ [100]}$, $\mathbf{V_L = 6.57 \cdot 10^5\ cm/s}$, $\mathbf{\Gamma = 0.15\ dB/(cm \cdot GHz^2)}$: $\mathbf{f_{low} \approx 1.971\ GHz}$ and $\mathbf{f_{up} \approx 2.108\ GHz}$.

3. $\mathbf{KRS-5\ [111]}$, $\mathbf{V_L = 1.92 \cdot 10^5\ cm/s}$, $\mathbf{\Gamma \approx 10\ dB/(cm \cdot GHz^2)}$: $\mathbf{f_{low} \approx 576\ MHz}$ and $\mathbf{f_{up} \approx 258\ MHz}$.

Here, $\mathbf{V_{SS}}$ and $\mathbf{V_L}$ are the slow shear acoustic mode and longitudinal one, respectively. They both are pure acoustic modes, providing exact coincidence between the wave vectors and the energy flow vectors with the chosen directions (in fact, with the acoustic axes in crystals) of these elastic waves propagation. The Bragg regime of light diffraction occurs with a large length $\mathbf{L}$ of acousto-optical interaction. In this case the dynamic acoustic grating is rather thick, so that during the analysis of diffraction one has to take account of the phase relations between waves in different orders. When the incident light beam is unlimited in a transverse direction, the reflected beam will be placed in the plane of incidence (i.e. in the $\mathbf{x_2 x_3}$-plane) and the angle of reflection should be equal to the angle $\mathbf{\theta_B}$ of incidence. The coupled-mode theory predicts that a considerable reflection of the incident light can be expected under condition

$$\mathbf{2k \sin\theta_B = mK = 2\pi m/\Lambda}, \tag{2.15}$$

where $\mathbf{k = 2\pi m/\lambda}$ is the light wavelengths, while $\mathbf{m}$ is the whole number, which reflects the $\mathbf{m-th}$ Fourier component of the perturbed dielectric permeability. In the case of pure sinusoidal profile peculiar to the acoustic wave, all the Fourier-components with $\mathbf{m \ge 2}$ will be equal to zero. Thus, the Bragg a regime can be realized only when the angle of light incidence $\mathbf{\theta_B}$ on a

thick dynamic acoustic grating meets the Bragg condition $\sin\theta_B = \lambda m/2\Lambda$ and inequality $Q = \lambda L/\Lambda^2 >> 1$ for the Klein-Cook parameter [2.6]. Usually, when an acoustic mode exited by the applied electric signal, the Bragg regime includes the incident and just one scattered light modes, whose normalized intensities are described by [2.7]

$$\text{a) } I_0 = \cos^2(q x_1), \qquad \text{b) } I_1 = \sin^2(q x_1),$$
$$\text{c) } q = \pi(\lambda \cos\theta_B)^{-1}\sqrt{M_2 P/2}, \qquad \text{d) } M_2 = n^6 p_{eff}^2/(\rho V^3), \qquad (2.16)$$

where x_1 is the space coordinate almost along the light propagation; P is the acoustic power density, ρ is the material density, p_{eff} is the effective photo-elastic constants for light scattering, and n is the averaged effective refractive index of a material. The Bragg regime is preferable for practical applications due to an opportunity to realize an 100% efficiency of light scattering by the acoustic wave. Taking the case of $x_1 = L$ in Eq.(2.16b) and $\cos\theta_B \approx 1$ in Eq.(2.16c), one can find from these equations that the acoustic power density P_0 needed for 100% efficiency of light diffraction into the first order can be estimated through the requirement $qL = \pi/2$ in Eq.(2.16b) as

$$P_0 = \frac{\lambda^2}{2L^2 M_2}. \qquad (2.17)$$

Thus, at the same values of optical wavelength λ and the interaction length L, the required acoustic power density will be inversely proportional to the acousto-optic figure of merit M_2. For the above-mentioned orientations of crystals, one can cite that [4,5]: (1) $M_2(Bi_{12}GeO_{20}\ [110],\ V_{SS}) = 5.17\cdot10^{-18}\ s^3/g$ and (2) $M_2(LiNbO_3,\ [100],\ V_L) = 7.0\cdot10^{-18}\ s^3/g$. For reaching 100% efficiency of operation at $\lambda = 500\ nm$ and $L = 1\ cm$, the following acoustic power densities P_0 can be found from Eq.(2.17): (1) $P_0(Bi_{12}GeO_{20}\ [110],\ V_{SS}) = 24.18\cdot10^7\ g/s^3 \approx 0.242\ W/mm^2$ and (2) $P_0\ (LiNbO_3,\ [100],\ V_L) = 17.86\cdot10^7\ g/s^3 \approx 0.179\ W/mm^2$.

It should be explained additionally: applying the needed electronic signals at the electronic input of AOC in such a way that the above-obtained levels of acoustic power density will be provided makes it possible physically and potentially technically to achieve 100% efficiency of control over the incident light diffraction. By the other words, instead of about 70% maximum efficiency shown in Fig.1 for traditional static diffraction gratings, involving the acousto-optical technique via creating the dynamic acousto-optical diffraction gratings is potentially able to provide close to 100% efficiency of dispersive element over all the range of the above-mentioned spectrum analysis.

The practical aspects of designing an updated version of the schematic arrangement for spectrometer under consideration lead first of all to creation of a modified optical scheme, which has to include some peculiarities of the AOC. Fig.2.4 represents the modified configuration of the spectrometer using

the AOC as dynamic diffraction grating instead of the static diffraction gratings; here, θ_B is the Bragg angle of light incidence for the chosen optical wavelength, see Eq.(2.15). The light coming from the telescope will pass through the spectrometer entrance slit at the focal plane of the collimator mirror, the reflected beam, a plane wave, will fall on to the AOC at the Bragg angle. Then, the diffracted beams corresponding to the first order will be imaged using a Schmidt-camera and analyzed. An additional modification is connected with the fact that the acousto-optical dynamic diffraction grating operates sufficiently effective in the Bragg transit regime instead of the reflection regime inherent in the above-mentioned classical spectrometer whose static diffraction gratings exhibit about **70%** maximum efficiency.

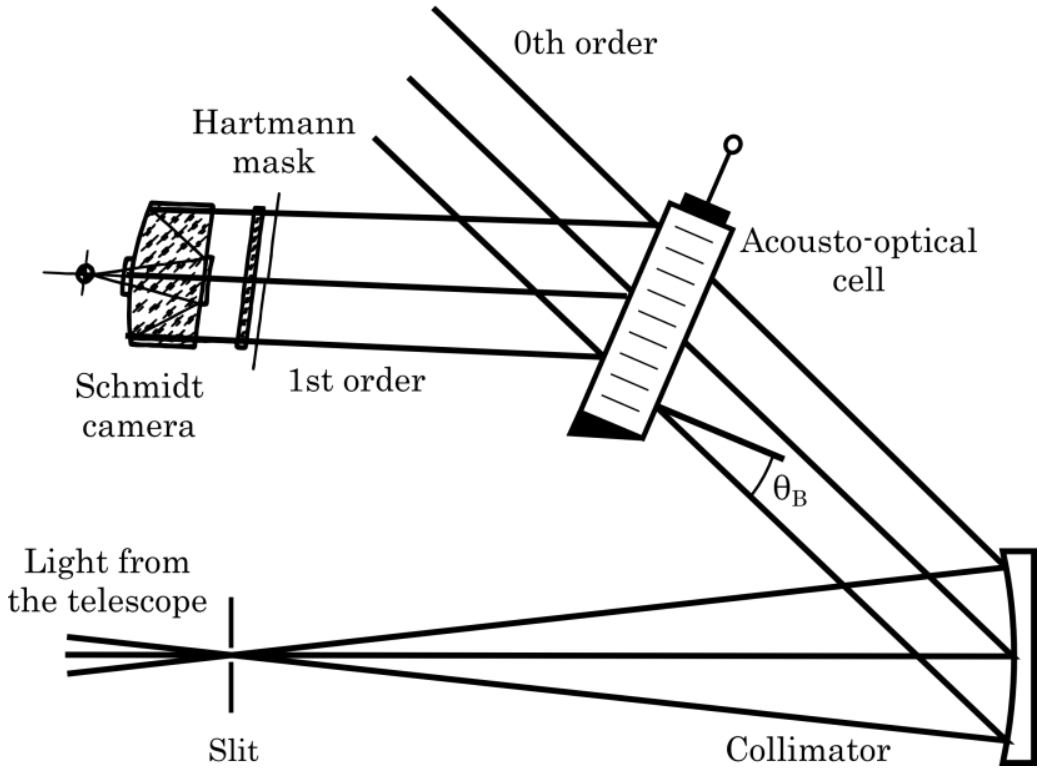

Figure 2.4. Layout for a new acousto-optical schematic arrangement inserted into the spectrometer; the proposed dispersive element, i.e. the dynamic diffraction grating is presented by acousto-optical cell operating in the transit regime of Bragg light diffraction.

2.4. Diffraction of the light beam of finite width by a harmonic acoustic wave at low acousto-optic efficiency

Schematic arrangement of the acousto-optical version of spectrometer, see Fig. 2.5, exhibits potential presence of optical beams whose widths are restricted due to condition of observations. This is why the diffraction of light beam of finite width by harmonic acoustic wave has to be reviewed and characterized. At first, to illustrate the existing physical tendency simpler let us start from a low acousto-optical efficiency approximation

$I_1 \approx (qx)^2 \sin^2(\eta x)/(\eta x)^2$, where now $\eta \neq 0$ is the angular-frequency mismatch. Due to almost orthogonal geometry of non-collinear acousto-optical interaction the angles of incidence θ_0 and diffraction θ_1 do not exceed usually about 10^0, so that one can use the simplified formulas

$$\text{a) } \theta_1 \approx \theta_0 + \frac{\lambda}{n\Lambda},$$

$$\text{b) } 2\eta(\theta_0, K) \approx K(\theta_0 - \theta_B),$$

$$\text{c) } \theta_B = -\frac{\lambda}{2nK} - \frac{(n_0 - n_1)K}{\lambda}, \qquad (2.17)$$

where n is the average refractive index; $n_{0,1}$ are the refractive indices for the incident or diffracted light, respectively.

Now, we assume that the area of propagation for a harmonic acoustic wave is bounded by two planes $x = 0$ and $x = L$ in a crystal. This acoustic wave has the amplitude function $u(z,t) = u_0 \exp[i(K_0 z - \Omega_0 t)]$ with the amplitude u_0, wave number K_0, and cyclic frequency Ω_0, and travels along z-axis. Then, let initially monochromatic light beam incidents on the area of interaction under the angle θ_0. At the plane $x = 0$, the light field is described by the complex valued amplitude function $e_{in}(z)$, reflecting the spatial structure of light field. The spectra of these fields are [2.8]

$$\text{a) } E_{in}(\theta_0) = \int_{-\infty}^{+\infty} e_{in}(z) \exp(-ik_0 z \sin\theta_0)\, dz,$$

$$\text{b) } U(K) = 2\pi u_0 \exp(-i\Omega_0 t)\, \delta(K_0 - K), \qquad (2.18)$$

where k_0 is the wave number of the incident light. Each individual component of the incident light beam is diffracted by the acoustic harmonic in the interaction area. Using Eqs.(2.17) and (2.18) within taken low acousto-optical efficiency, the angular spectrum of the diffracted light can be written as [2.9]

$$E_D(\theta_1) = \exp(-i\Omega_0 t) \times \int_{-\infty}^{\infty} \left\{ E_{in}(\theta_0) T(\theta_0, \theta_B) \delta\left(\theta_1 - \frac{\lambda K_0}{2\pi n} - \theta_0\right) \right\} d\theta_0, \qquad (2.19)$$

$$T(\theta_0, \theta_B) = (qL) \cdot \frac{\sin[\eta L]}{\eta L} = (qL) \cdot \frac{\sin[K_0 L(\theta_0 - \theta_B)/2]}{K_0 L(\theta_0 - \theta_B)/2}. \qquad (2.20)$$

Equation (2.19) describes AOC as linear optical system with the transmission function $T(\theta_0, \theta_B)$, which is real-valued (and positive) within its bandwidth, i.e. AOC does not insert phase perturbations in the spectrum of optical signal.

When the width D_{in} of the incident light beam is less than acoustic aperture of AOC, one can say that acoustic beam is infinitely wide, while light beam is described by the complex amplitude function $e_{in}(z) = e_0\, \mathrm{rect}(z/D_{in})$, where

$\mathbf{rect}(\xi)=1$ only when $|\xi|\le 1/2$ and $\mathbf{rect}(\xi)=0$ when $|\xi|>1/2$. Its angular Fourier spectrum is given by

$$\mathbf{E_{in}}(\theta_0)=(e_0 D)\cdot\frac{\sin[\pi n D_{in}(\theta_0-\theta_B)/\lambda]}{\pi n D_{in}(\theta_0-\theta_B)/\lambda}. \qquad (2.21)$$

Substituting Eq.(2.21) in Eq.(2.19), one can obtain angular distribution for the diffracted light intensity at low acousto-optical efficiency.

$$\begin{aligned}
&\text{a)}\ \mathbf{I_D}(\theta_1)=\left|\mathbf{E_D}(\theta_1)\right|^2=(q^2L^2e_0^2D_{in}^2)\cdot S_0^2\cdot T_0^2\ ,\\
&\text{b)}\ S_0^2=\frac{\sin^2\left\{\pi n D_{in}\lambda^{-1}\left[\theta_1-\theta_0-\lambda/(n\Lambda_0)\right]\right\}}{\left\{\pi n D_{in}\lambda^{-1}\left[\theta_1-\theta_0-\lambda/(n\Lambda_0)\right]\right\}^2}\ ,\\
&\text{c)}\ T_0^2=\frac{\sin^2\left\{\pi L\Lambda_0^{-1}\left[\theta_1-\theta_B-\lambda/(n\Lambda_0)\right]\right\}}{\left\{\pi L\Lambda_0^{-1}\left[\theta_1-\theta_B-\lambda/(n\Lambda_0)\right]\right\}^2}.
\end{aligned} \qquad (2.22)$$

The functions S_0^2 and T_0^2 represent angular spectra of light and acoustic beams. The diffracted light structure is determined by overlapping the functions S_0^2 and T_0^2, i.e. by relation between the light divergence angle $\varphi_L=\lambda/nD_{in}$ and the acoustic one $\varphi_S=\Lambda_0/L$, so that the Gordon parameter $G=\varphi_L/\varphi_S$ had been introduced [2.10]. With $G\approx 1$, the widths of S_0^2 and T_0^2 have the same order. When $G<<1$ ($\varphi_L<<\varphi_S$), one can simplify Eq.(2.22a) as $\mathbf{I_D}(\theta_1)\approx(q^2L^2e_0^2D_{in}^2)\cdot S_0^2$; with $G>>1$ ($\varphi_L>>\varphi_S$), one yields $\mathbf{I_D}(\theta_1)\approx(q^2L^2e_0^2D_{in}^2)\cdot T_0^2$. These peculiarities of diffracting light beam of finite width are illustrated by Fig. 2.5. The diffracted light waves take their origin in all the points of overlapping light and acoustic beams. Due to their interference, these waves shape the diffracted light beam, propagating at the angle $\theta=\lambda/n\Lambda_0$. The diffracted light width D_D can be estimated by

$$D_D=[D_{in}\cos^{-1}\theta_0+2\tan(\theta/2)]\cos(\theta-\theta_0)\approx D_{in}+\lambda L/(n\Lambda_0)$$

This relation can be rewritten as $\varphi_D^{-1}\approx\varphi_L^{-1}+\varphi_S^{-1}$, where $\varphi_D=\lambda/(nD_D)$. Thus the divergence angle of the diffracted light is close (in its order of quantity) to the smallest divergence angle of the interacting beams.

The acousto-optic efficiency ν can be determined as ratio of the diffracted light intensity to the incident light intensity when both $|\mathbf{E_{in}}(\theta_0)|^2$ and $\mathbf{I_D}(\theta_1)$ from Eqs.(2.21) and (2.22a) will be integrated over the corresponding angle ranges:

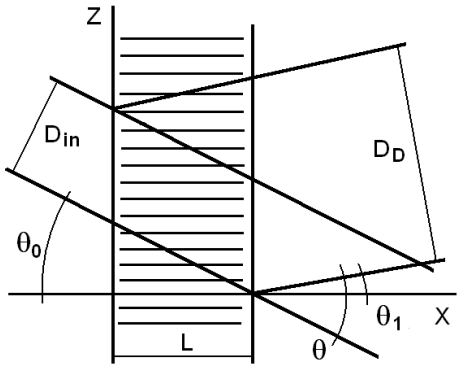

Figure 2.5. Geometry of interaction between light and acoustic beams

$$\nu = q^2 L^2 \left(e_0^2 D_{in}^2 \int_{-\pi/2}^{\pi/2} S_0^2 T_0^2 \, d\theta_1 \right) = q^2 L^2 B(G). \qquad (2.23)$$

Efficiency of diffraction for the plane incident light wave has maximum efficiency at $\theta_0 = \theta_B$, and the term q^2L^2, describing the acousto-optical efficiency for plane incident light wave, is marked out here to highlight the contribution of light beam finiteness. However, Bragg condition cannot be provided now for all the angular components described by Eq.(2.21). This is why one can chose the angle of incidence θ_0 in such a way that the phase synchronism condition will be satisfied for the axis-component of incident beam. In the case of S_0^2 with $\theta_0 = \theta_B$, one can obtain [2.11], see Fig. 2.6.

$$B(G) = \begin{cases} (3G-1)/(3G^2), G \geq 1 \\ 1-(G/3), G \leq 1 \end{cases} \qquad (2.24)$$

Equation (2.23) should be compared with the above taken relative intensity of diffraction $I_1 \approx (qL)^2$ for plane optical waves at low acousto-optical efficiency. One can see from Eq.(2.23) that a finite width of the incident light beam leads to appearing an additional factor $B(G)$ depending only on the Gordon parameter $G = \varphi_L / \varphi_S$. The factor $B(G)$ reaches unity only in the limit of $G \to 0$, which corresponds to the case of plane incident light wave. Growing the Gordon parameter makes acousto-optical interaction worse. Physically, this effect is motivated by the fact that exact phase synchronism can be realized only for one, namely, axis-component of light beam, while all other components are diffracted with lower efficiency.

Within Bragg diffraction of a high acousto-optical efficiency, the factor q, conditioned by acoustic power density P via Eq.(10c), has to be taken into account. The transmission function $T(\theta_0, \theta_B)$ from Eq.(2.20) should be substituted by

$$T_B(q, \theta_0, \theta_B) = (qL) \cdot \frac{\sin[L\sqrt{q^2 + K_0^2(\theta_0 - \theta_B)^2/4}]}{[L\sqrt{q^2 + K_0^2(\theta_0 - \theta_B)^2/4}]}, \qquad (2.25)$$

This modification leads ultimately to another expression for efficiency $\nu_B = \sin^2(qL)\cdot B_B(q,G)$, which is similar to Eq.(2.23). As before, the term $\sin^2(qL)$, describing the diffraction of high efficiency for plane incident light wave, is marked out to exhibit the contribution of light beam finiteness, while the function $B_B(q,G)$ reflects the same tendency as $B(G)$. Anyway, finally one can conclude that when AOC operates over the light beams of finite width, decreasing the acousto-optical efficiency due to partial asynchronism for the divergent incident light beam cannot be eliminated.

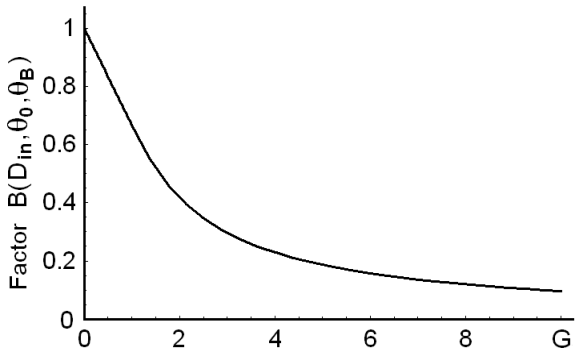

Figure 2.6. The factor $B(G)$ versus the Gordon parameter $G = \varphi_L / \varphi_S$.

2.5. Conclusions

It was suggested exploiting an acousto-optical cell (AOC) as a dispersive element in Optical spectrometer of the Guillermo Haro astrophysical observatory (Mexico) [2.12, 2.13]. Potentially, involving acousto-optical technique, which can realize tuning both the spectral resolution and the range of observation electronically, makes possible eliminating the above-mentioned practical demerits. The requirements to the cell combine a large optical aperture with the needed slit-density and possibly high efficiency of operation under an acceptable acoustic power. This is why initially one have restricted the problem by the slit-density **300 lines/mm**. The analysis has show that at least the following materials can be used for designing similar cell. It can be lithium niobate ($LiNbO_3$)-crystal excited by the longitudinal acoustic mode along the **[100]**-axis at the frequency **2 GHz**. This selection gives **300 lines/mm** with total losses **~5.4 dB/aperture**. Then, one can consider bismuth germanate ($Bi_{12}GeO_{20}$)-crystal using the shear acoustic mode along the **[110]**-axis at **0.53 GHz**, so that the slit-density **300 lines/mm** appears with the losses **~6.3 dB/aperture**. The neighboring figures of acousto-optical merit for these materials promise desirable efficiencies of operation, so that even close to **100%** efficiency peculiar to the dynamic acousto-optical dispersive element over all the range of the spectrum analysis can be expected. The potential performance of the described grating will be within the most requested resolutions and range of wavelengths ($400-1000\,nm$) at the Guillermo Haro astrophysical observatory. Finally, diffracting the light beam of finite width by a harmonic acoustic wave at low acousto-optic efficiency have been briefly discussed.

Chapter 3

Transmission Function of Advanced Collinear Acousto-Optical Filter

An opportunity for exploiting specific mechanism of the acousto-optic nonlinearity to regulate performances of the collinear acousto-optical filter, realizing the sequential spectrum analysis of optical signals, is considered. This possibility is theoretically analyzed and confirmed experimentally with an advanced filter based on calcium molybdate ($CaMoO_4$) single-crystal with a $15-$microsecond time-aperture. It is able to operate over red and near-infrared light at relatively low radio-wave frequencies providing almost lossless regime for the controlling acoustic waves of the finite amplitude. Under certain conditions, the transmission function of electronically tunable filter exhibits a marked dependence on the applied acoustic power density, and as a result, one can significantly squeeze the transmission function, i.e. in fact improve the spectral resolution of this filter at the cost of decreasing the device efficiency partially. The identified and observed non-linear effect makes possible varying the performance data of similar advanced collinear acousto-optical filter governed by external signals of the finite amplitude.

3.1. Theory and Operation

In 1970 – 80s, novel optical spectral devices, electronically tunable acousto-optical filters (AOFs) had been proposed and developed. During the years gone the AOFs have been remarkably progressed, and now they are widely exploited, for instance, in modern astrophysical observations [3.1, 3.2]. Schematically, the AOFs can be separated on collinear and non-collinear filters, depending on the relative directions of passing the waves through crystalline cell within their geometric arrangements, as well as on sequential and parallel devices, depending on the algorithms realizing for spectrum analysis of optical signals. Their features are characterized by the amplitude and spectral parameters. Collinear acousto-optical interaction by itself had

been initially predicted and studied in the middle of sixties by R.W. Dixon [3.3] and then, starting from the seventies has been successfully exploited in various applications, among which first of all one ought to call the collinear tunable acousto-optical filters [3.4–8]. The conventional analysis of this phenomenon in terms of lossless plane waves was presented in a number of classical issues [3.9, 3.10]. Practically, the methods of acousto-optics had manifested themselves as rather effective due to their property of quantum mechanic amplification resulting in the control over high-energetic photons by low-energetic phonons. The corresponding gain is represented by the direct ratio of the scattered photon frequency to a frequency of the controlling phonon frequency. It allows practical application of a given acoustic field approximation or the regime of a weak coupling, when the spatial distribution of acoustic beam is almost independent on the spatial distribution of light that leads to considerable theoretical and practical facilities. In particular, 100% efficiency of light scattering may be achieved without any effect on the acoustic beam, so the above-mentioned control can be repeated for a lot of times with low losses of acoustic energy. Moreover, an essential difference between velocities of light and ultrasound gives us an opportunity for applying the quasi-stationary approximation to the analysis of modern acousto-optical problems. In the past decades great progress has been made in acousto-optics and now it is a widely used technique in the field of data processing [3.11]. Nevertheless, recently the existence of a new branch in studies and applications of collinear acousto-optical interaction, which is associated with acousto-optical nonlinearity, for example, in the form of three-wave coupled states, has been manifested [3.12, 3.13]. That is why it is a worthwhile investment to develop this line more, because the objects being under consideration here are closely connected with the above-mentioned nonlinearity in the regime of a weak coupling. Within this consideration, the exact and closed analytical model of the collinear light scattering by continuous acoustic waves of the finite amplitude in a birefringent lossless material is developed. Similar approach definitely includes practically important case of the presence of really small acoustic attenuation in widely used acousto-optical filters operating in the traveling-wave regime at relatively low radio-frequency acoustic waves and exploiting such materials as quartz or calcium molybdate single crystals. In so doing, the peculiarities of the effect conditioned by the acousto-optical nonlinearity are analyzed, which leads to a measurable dependence of the transmission function and consequently, the spectral resolution peculiar to this filter, on the applied power density of acoustic waves of finite amplitude in a way allowing, for instance, to improve the spectral resolution of similar device at the cost of partial demerit for the filter efficiency.

3.2. Three Wave Collinear Interaction

A three-wave co-directional collinear interaction with the mismatched wave numbers in a two-mode lossless medium is described by a set of three nonlinear partial differential equations. Here, the regime of a weak coupling is considered [3.12, 3.13], when two light modes are scattered by relatively slow wave, being non-optical by its nature, when essentially effective Bragg scattering of light can be achieved without any observable influence of the

scattering process on that non-optical wave, because the number of interacting photons is a few orders less than the number of the scattering quanta injected into a medium. Then, the velocities of light modes can be approximated by the same value c, because usually the length of crystalline materials does not exceed $20\,cm$. In this regime, the above-mentioned set of equations falls into an independent equation for the complex amplitude $U(x,t)$ of a slow wave (V is the velocity of this wave) and a pair of the combined equations for the complex amplitudes $C_0(x,t)$ and $C_1(x,t)$ of the incident (pumping) light wave and scattered one, respectively,

$$\text{a)}\ \frac{\partial U}{\partial x}+\frac{1}{V}\frac{\partial U}{\partial t}=0,\qquad \text{b)}\ \frac{\partial C_0}{\partial x}+\frac{1}{c}\frac{\partial C_0}{\partial t}=-q_1\,C_1U^*\exp(2i\eta x),$$
$$\text{c)}\ \frac{\partial C_1}{\partial x}+\frac{1}{c}\frac{\partial C_1}{\partial t}=q_0\,C_0U\exp(-2i\eta x). \tag{3.1}$$

Here, $q_{0,1}$ are the constants of interaction and 2η is the mismatch of wave numbers inherent in the interacting light waves. Now, the tracking coordinates $(x,\tau=t-x/c)$ are taken into account and assume that non-optical wave, governed by Eq.(3.1a) and described by $U=u[x(1-V/c)-V\tau]\exp(i\varphi)$, has the constant phase φ, so that one can convert Eqs.(3.1b) and (3.1c) into equations of the second order

$$\frac{\partial^2 C_{0,1}}{\partial x^2}-\left(\frac{1}{u}\frac{\partial u}{\partial x}\pm 2i\eta\right)\frac{\partial C_{0,1}}{\partial x}+q_0\,q_1\,u^2\,C_{0,1}=0. \tag{3.2}$$

with the condition $C_{0,1}=a_{0,1}(x,t)\exp[i\Phi_{0,1}(x,t)]$, $\gamma_{0,1}=\partial\Phi_{0,1}/\partial x$ and then divide real and imaginary parts in Eqs.(3.2) as

$$\frac{\partial^2 a_{0,1}}{\partial x^2}-\frac{1}{u}\frac{\partial u}{\partial x}\frac{\partial a_{0,1}}{\partial x}+\left[q_0\,q_1\,u^2-\gamma_{0,1}^2\pm 2\eta\gamma_{0,1}\right]a_{0,1}=0, \tag{3.3}$$

$$2\left(\gamma_{0,1}\mp\eta\right)\frac{\partial a_{0,1}}{\partial x}+\left(\frac{\partial\gamma_{0,1}}{\partial x}-\frac{\gamma_{0,1}}{u}\frac{\partial u}{\partial x}\right)a_{0,1}=0. \tag{3.4}$$

Equations (3.4) have the following general solutions

$$\gamma_{0,1}=\pm\eta\,u\,a_{0,1}^{-2}\int u^{-1}\left(\partial a_{0,1}^2/\partial x\right)\,dx+\Gamma_{0,1}\,u\,a_{0,1}^{-2}, \tag{3.5}$$

where $\Gamma_{0,1}$ are the integration constants. The analysis shows that the collinear light scattering with $\Gamma_{0,1}\neq 0$ leads to appearing optical backgrounds. Within further analysis here, the only regime with $\Gamma_{0,1}=0$ will be considered in a view of potential application to filtering optical beams without backgrounds.

Choosing the simplest case of $\Gamma_{0,1}=0$ in Eqs.(3.5), one can study the phenomenon in the continuous-wave regime for both the incident light and the non-optical wave when $u[x(1-V/c)-V\tau]=U_0$ is constant. Equations (3.3) and (3.4) are analyzed with the fixed magnitude of the mismatch η and

natural for practice the boundary conditions $a_0(x=0,t)=1$, $(\partial a_0/\partial x)(x=0,t)=0$, $a_1(x=0,t)=0$, $(\partial a_1/\partial x)(x=0,t)=q_0 U_0$ in a half-infinite medium. In so doing, one yields $\gamma_{0,1}=\pm\eta$ and $-\gamma_{0,1}^2 \pm 2\eta\gamma_{0,1}=\eta^2$. Thus, with the parameter $q_0 q_1 U_0^2=\sigma^2$, characterizing physically contributions of both the material properties and the power density of non-optical wave, Eqs.(3.3) take the form

$$\frac{\partial^2 a_{0,1}}{\partial x^2}+(\sigma^2+\eta^2)\, a_{0,1}=0. \tag{3.6}$$

To construct the solution, which can be easily used in practically important cases of significant phase mismatches the conservation law $q_0 a_0^2+q_1 a_1^2=q_0$ - const is used, resulting from Eqs.(3.1). Combining Eqs.(3.6) for a_0 and a_1, one can obtain a pair of the following equations

$$\frac{\partial(a_{0,1}^2)}{\partial x}=2\sqrt{a_{0,1}^2(q_{0,1}^{-1}q_0-a_{0,1}^2)(\sigma^2+\eta^2)}, \tag{3.7}$$

whose solutions with arbitrary integration constants $\theta_{0,1}$ are given by

$$\text{a)}\ a_{0,1}^2=q_{0,1}^{-1}q_0\sin^2\left[\theta_{0,1}+G(x)\right], \qquad \text{b)}\ G(x)=x\sqrt{\sigma^2+\eta^2}. \tag{3.8}$$

Using the above-noted boundary conditions, one arrives at

$$\text{a)}\ \theta_0=\arcsin\left[\sigma^{-1}\sqrt{\sigma^2+\eta^2}\right], \qquad \text{b)}\ \theta_1=0\ ,. \tag{3.9}$$

so that the stationary intensities of the pumping and scattered light waves can be expressed as

$$\text{a)}\quad |C_0(x)|^2=\frac{\eta^2}{\sigma^2+\eta^2}+\frac{\sigma^2}{\sigma^2+\eta^2}\cos^2\left[G(x)\right],$$

$$\text{b)}\quad |C_1(x)|^2=\frac{q_0}{q_1}\frac{\sigma^2}{\sigma^2+\eta^2}\sin^2\left[G(x)\right]. \tag{3.10}$$

These solutions include contributions of two types. The first summand in the intensity $|C_0|^2$ represents a background determined by the mismatch η; the second one gives the oscillations imposed on that background. The scattered light wave contains only oscillations without a background due to the above-chosen restriction $\Gamma_{0,1}=0$.

3.3. Efficiency of Collinear Interaction in $CaMoO_4$

Now let us consider a few practically useful estimations related to experimental observation of the collinear acousto-optical interaction with linear acoustic losses in a birefringent cell made of a calcium molybdate ($CaMoO_4$) single crystal. In this particular case, one can observe only

anomalous process of light scattering, so that the parameters $q_{0,1}$ are described [3.9] by

$$q_{0,1} = \frac{\left|\vec{k}_{0,1}\right|}{4n^2_{0,1}} (\tilde{\vec{e}}_0 \, \Delta\varepsilon \, \vec{e}_1) \, . \qquad (3.11)$$

Here, $n_{0,1}$ are the refractive indices for the interacting light waves, $\left|\vec{k}_{0,1}\right| = 2\pi n_{0,1}/\lambda$, λ is the light wavelength in a vacuum, and the last term in brackets, describing the efficiency of interaction, is subject to find. This term includes the eigen-orts $\vec{e}_{0,1}$ of polarizations for the incident and scattered light beams as well as the tensor $\Delta\varepsilon$ of perturbations of the dielectric permittivity under action of the acoustic wave in a medium. To estimate the efficiency of interaction, i.e. to find the contribution of brackets to Eq.(3.11), the acoustic modes with the wave unit-vector $\vec{m}$ oriented along the **[100]**-axis are considered, so that $\vec{k}_{0,1} = \vec{m}\left|\vec{k}_{0,1}\right|$. In this case, the longitudinal mode gives zero efficiency of interaction due to the symmetry of $CaMoO_4$-crystal, while the contribution from the shear mode with its unit-vector $\vec{u}$ of the transversal elastic displacements oriented along the **[001]**-axis, i.e. with $\vec{u} = [0,0,1]$, has to be calculated. Thus, one can write the deformation tensor γ and the unperturbed dielectric permittivity tensor ε in the main crystallographic axes as

$$\text{a)} \quad \gamma = \frac{\gamma_0}{2}\left(\vec{u}\cdot\vec{m} + \vec{m}\cdot\vec{u}\right) = \frac{\gamma_0}{2}\begin{pmatrix} 0 & 0 & 1 \\ 0 & 0 & 0 \\ 1 & 0 & 0 \end{pmatrix}, \qquad \text{b)} \quad \varepsilon = \begin{pmatrix} \varepsilon_0 & 0 & 0 \\ 0 & \varepsilon_0 & 0 \\ 0 & 0 & \varepsilon_e \end{pmatrix} . \qquad (3.12)$$

Here, γ_0 is the amplitude of the shear deformation, while $\varepsilon_0 = n_0^2$ and $\varepsilon_e = n_e^2$ are the eigen-values of the unperturbed dielectric permittivity tensor ε. Now, the tensor γ of the second rank with the components γ_{kl} $(k,l=1,2,3)$ can be converted into a 6-dimension vector $\bar{\gamma} = \gamma_0(0,0,0,0,1,0)$ with the components $\bar{\gamma}_\mu$ $(\mu = 1,\cdots,6)$ using the standard procedure [3.14], which includes re-notating $\bar{\gamma}_\mu = \gamma_{kk}$ $(\mu = 1,2,3)$ and $\bar{\gamma}_\mu = 2\gamma_{kl}$ $(k \neq l, \mu = 4,5,6)$. If now one will use the same procedure [3.14] and take the photo-elastic tensor p of the fourth rank for a calcium molybdate single crystal in the form of a 6×6 matrix $\hat{p}$, it will be allowed first to construct and to calculate the product $\hat{p}\bar{\gamma} = \gamma_0(0,0,0,p_{45},p_{44},0)$, and then to convert the result back to the form of a standard tensor $(p\gamma)$ of the second rank.

The next step of the analysis is connected with finding the dielectric permittivity perturbations tensor $\Delta\varepsilon$, whose components can be written as $\Delta\varepsilon_{ij} = \varepsilon_{im}\varepsilon_{nj}p_{mnkl}\gamma_{kl}$ [3.9]. In the particular case of a $CaMoO_4$-crystal whose point symmetry group is 4/m, one can write [3.14 - 16]:

$$p_{\lambda\mu} = \begin{pmatrix} p_{11} & p_{12} & p_{13} & 0 & 0 & p_{16} \\ p_{12} & p_{11} & p_{13} & 0 & 0 & -p_{16} \\ p_{31} & p_{31} & p_{33} & 0 & 0 & 0 \\ 0 & 0 & 0 & p_{44} & p_{45} & 0 \\ 0 & 0 & 0 & -p_{45} & p_{44} & 0 \\ p_{61} & -p_{61} & 0 & 0 & 0 & p_{66} \end{pmatrix}$$

$$= \begin{pmatrix} 0.17 & -0.15 & -0.08 & 0 & 0 & 0.03 \\ -0.15 & 0.17 & -0.08 & 0 & 0 & -0.03 \\ 0.10 & 0.10 & 0.08 & 0 & 0 & 0 \\ 0 & 0 & 0 & 0.06 & 0.06 & 0 \\ 0 & 0 & 0 & -0.06 & 0.06 & 0 \\ 0.10 & -0.10 & 0 & 0 & 0 & 0.03 \end{pmatrix}. \qquad (3.13)$$

The result of calculating has the form

$$\Delta\varepsilon = \gamma_0 \varepsilon_0 \varepsilon_e \begin{pmatrix} 0 & 0 & p_{44} \\ 0 & 0 & p_{45} \\ p_{44} & p_{45} & 0 \end{pmatrix}. \qquad (3.14)$$

Now, the orts $\vec{e}_{0,1}$ of polarization for the incident and scattered light waves are taken into account. When the wave vectors of these light waves are collinear to the wave normal ort $\vec{m}$ for the acoustic wave and, of course, to the **[100]**-axis in calcium molybdate crystal, the eigen-orts $\vec{e}_{0,1}$, of light polarizations should be oriented, as it directly follows from Eq.(3.12b), along the **[010]** and **[001]** axes, so that one can take, for example, $\vec{e}_0 = [0,1,0]$ and $\vec{e}_1 = [0,0,1]$ with $n_0 = n_o$ and $n_1 = n_e$. As a result, one can obtain the contribution of brackets to Eq.(3.11) as

$$\tilde{\vec{e}}_0 \, \Delta\varepsilon \, \vec{e}_1 = \tilde{\vec{e}}_1 \, \Delta\varepsilon \, \vec{e}_0 = \gamma_0 \varepsilon_0 \varepsilon_e p_{45}. \qquad (3.15)$$

In so doing, one can find that $q_{0,1} = \pi(2\lambda)^{-1} n_{e,o} \gamma_0 n_{o,e}^2 p_{45}$. One can see now that the difference between q_0 and q_1 is rather small, because $q_0/q_1 = n_e/n_o$. Then, because the amplitude of deformation can be explained as $\gamma_0 = \sqrt{2P/(\rho V^3)}$, where P is the acoustic power density, one can finally obtain

$$\text{a)} \quad q_0 = \frac{\pi}{\lambda}\sqrt{\frac{P}{2}\left(\frac{n_e^2 n_o^4 p_{45}^2}{\rho V^3}\right)}, \qquad \text{b)} \quad q_1 = \frac{\pi}{\lambda}\sqrt{\frac{P}{2}\left(\frac{n_o^2 n_e^4 p_{45}^2}{\rho V^3}\right)}. \qquad (3.16)$$

It should be noted that the factors taken in brackets in Eqs.(3.16) represent the figure of acousto-optical merit peculiar to estimating the efficiency of crystalline materials in acousto-optics [3.17] , while the refractive indices are slightly dispersive in behavior, see Table 1.

At this step, a few numerical estimations inherent in the collinear interaction under consideration at the light wavelength of $\lambda = 671\,\mathrm{nm}$ in the $CaMoO_4$-crystalline cell are ready to be performed. Taking the material density $\rho = 4.34\,\mathrm{g/cm^3}$, acoustic velocity $V = 2.95\cdot10^5\,\mathrm{cm/s}$, $p_{45} = 0.06$, $n_e = 1.9889$, $n_o = 1.9811$, and $\Delta n = 0.0078$ at the chosen light wavelength [3.18], one can calculate the figure of acousto-optical merit $M_2 = n_o^3 n_e^3 p^2 (\rho V^3)^{-1}$, where p is an effective photo-elastic constant, and ρ is the crystal density, as $M_2 \approx 1.977\cdot10^{-18}\,(s^3/g)$ with an accuracy of about 1%.

3.4. Resolution of $CaMoO_4$ Filter

3.4.1.Traditional Approach

As previously mentioned the spectral resolution $\delta\lambda$ and the frequency resolution δf of collinear acousto-optical filters are usually estimated as $|\delta\lambda| = (\lambda/f_0)\,\delta f$ and $\delta f = V/L$, where f_0 and V are the carrier frequency and velocity of acoustic wave; L is the longitudinal aperture of filter, i.e. the length of acousto-optical interaction. It is obviously seen that these formulas do not include potential influence of the initial acoustic power density on the resolution.

At first, let us consider Eqs.(3.13b) and (3.15b) for the lossless medium in the case of infinitely small signals, i.e. with $\sigma \to 0$. In so doing, one can estimate $G(x) = \eta x$, $G(0) = 0$, and write

$$|C_1(x)|^2 = \left(\frac{q_0\,(\sigma x)^2}{q_1} \right) \cdot \frac{\sin^2(\eta x)}{(\eta x)^2}\,, \qquad (3.17)$$

where the distance x can be considered as a parameter. Historically, estimating the resolution is connected with the well-known Rayleigh criterion, which predicts in fact separating a pair of the neighboring $(\sin u/u)^2$ – shaped distributions at the intensity level of $\nu \approx 0.4053$. This is exactly the case of Eq.(3.17), and one has to resolve the transcendent algebraic equation $\sin(\eta x) = \nu^{1/2}(\eta x) \approx 0.6368\,(\eta x)$. The first (both positive and negative) solutions to this algebraic equations are $\eta_{(\pm)} x = \pm\pi/2$. They lead to the bandwidth from $\eta_{(-)} x = -\pi/2$ to $\eta_{(+)} x = +\pi/2$, i.e. to the full bandwidth at the intensity level: $\nu \approx 0.4053$ $\Delta\eta x = \eta_{(-)} x + \eta_{(+)} x = |-\pi/2| + |+\pi/2| = \pi$. Together with this a one-side mismatch η had been previously [see Eqs.(3.1)] determined as $\eta = \Delta K/2 = \pi\delta f/V$, so that in the more detailed form $\eta_{(\pm)} = \pi\delta f_{(\pm)}/V$ (where $\delta f_{(\pm)}$ are the corresponding one-side frequency deviations) and consequently, the total deviation of the mismatch is given by $\Delta\eta = \eta_{(-)} + \eta_{(+)} = \pi(\delta f_{(-)} + \delta f_{(+)})/V = \pi\delta f/V$. Combining the expressions, which include $\Delta\eta$, one arrives at the above-noted formula $\delta f = V/x$, where one can

undoubtedly put $x = L$. Thus, one can see that full width of the main lobe inherent in a $(\sin u/u)^2$ – shaped distribution at the intensity level $\nu \approx 0.4053$ gives the "standard" determination of the frequency resolution in acousto-optics, which is conditioned by the limit $\sigma \to 0$.

3.4.2.Loss-Less Medium Case

Now, lets consider Eqs.(3.8b) and (3.10b) in the lossless case with signals of finite amplitude when $\sigma \neq 0$. Because of $G(x) = x\sqrt{\sigma^2 + \eta^2}$ and $G(0) = 0$, one can write

$$|C_1|^2 = \left(\frac{q_0}{q_1}\right) \frac{(\sigma x)^2}{(\sigma x)^2 + (\eta x)^2} \sin^2\left[\sqrt{(\sigma x)^2 + (\eta x)^2}\right]. \qquad (3.18)$$

To estimate the frequency resolution at the above-noted intensity level $\nu \approx 0.4053$ Eq.(3.17) has to be normalized as

$$\frac{|C_1|^2}{|C_1(\eta = 0)|^2} = \left[\frac{(\sigma x)^2}{(\sigma x)^2 + (\eta x)^2}\right] \cdot \frac{\sin^2\left[\sqrt{(\sigma x)^2 + (\eta x)^2}\right]}{\sin^2(\sigma x)}. \qquad (3.19)$$

The 3D-plots inherent in these distributions are presented in Fig. 3.1 for the scattered light intensity $|C_1(x)|^2$ in absolute units, see Eq.(3.18), and for the normalized intensity from Eq.(3.19) in practically reasonable approximation $q_0/q_1 \approx 1$. Fig. 3.1a gets the interval $0 \le \sigma x < 3\pi$ and illustrates a regular structure in absolute units, which exhibits reaching a sequence of unit-valued maxima along the line $\eta x = 0$ with a dimensionless period $\sigma x = \pi$. Fig. 3.1b reflects the normalized distribution on the smaller interval $0 \le \sigma x \le \pi$ and includes the level $\nu \approx 0.4053$-plane for estimating the width in terms of a one-side dimensionless mismatch ηx.

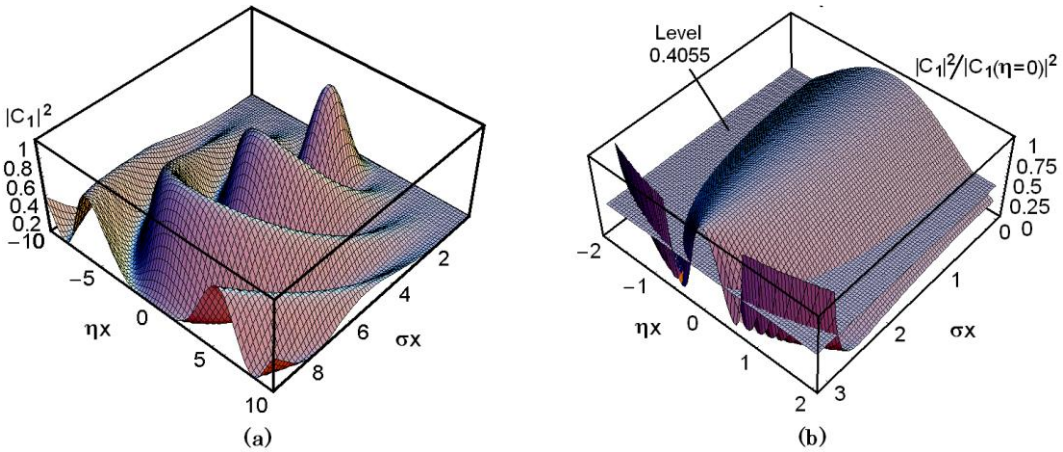

Figure 3.1. The 3D-plots of the scattered light intensity profile with $q_0/q_1 \approx 1$: (a) for the absolute values on the interval $0 \le \sigma x < 3\pi$ and (b) for the normalized distribution on the interval $0 \le \sigma x \le \pi$

A set of 2D-plots for the scattered light intensity $\left|\mathbf{C_1[(\sigma x),(\eta x)]}\right|^2$ is presented in Figs. 3.2 in the absolute form for the range of products $\mathbf{1.0 \le \sigma x < \pi}$ in the same approximation $\mathbf{q_0 / q_1 \approx 1}$. These 2D-plots illustrate in details the dynamics of evolving the distributions step by step and confirm that one can expect narrowing the normalized intensity profile noted by Eq.(3.19) with $\mathbf{\sigma x \to \pi}$ from smaller values as depicted in Fig.3.1b.

With $\mathbf{1.0 \le \sigma x < \pi}$, estimations at the above-chosen intensity level $\mathbf{\nu \approx 0.4053}$ give one-side mismatches $\mathbf{\eta x(\sigma x = 1.0) = 1.511}$, $\mathbf{\eta x(\sigma x = \pi/2) = 1.414}$, $\mathbf{\eta x(\sigma x = 2.0) = 1.292}$, $\mathbf{\eta x(\sigma x = 2.5) = 1.059}$, and $\mathbf{\eta x(\sigma x = 3.0) = 0.524}$, see Fig.3.2b, which lead to the corresponding full bandwidths $\mathbf{\Delta\eta x(\sigma x) = 2\eta x(\sigma x)}$. These numbers should be compared with the previously obtained a one-side mismatch estimation $\mathbf{\eta x(\sigma x \to 0) = \pi/2 \approx 1.5708}$ and the full bandwidth $\mathbf{\Delta\eta x(\sigma x \to 0) = \pi}$, corresponding to relatively low efficiency of light scattering in the regime of a given incident optical field approximation. One can see from these estimations and Fig. 3.2 that the contribution from acoustic wave of the finite amplitude narrows the profiles, and the most efficient regime, providing theoretically $\mathbf{100\%}$ efficiency of light scattering, can be achieved with $\mathbf{\sigma x = \pi/2}$, see Fig.3.2a, when the profile width will be about $\mathbf{10\%}$ better than in the case of a low-power non-optical wave. Growing the product $\mathbf{\sigma x}$ makes it possible to narrow profile for more, but at the cost of decreasing the efficiency significantly, see Fig 3.3. Nevertheless, a desirable balance between the contour width and efficiency can be found here, for instance in vicinity of $\mathbf{\sigma x \cong 2.0}$, if the case requires.

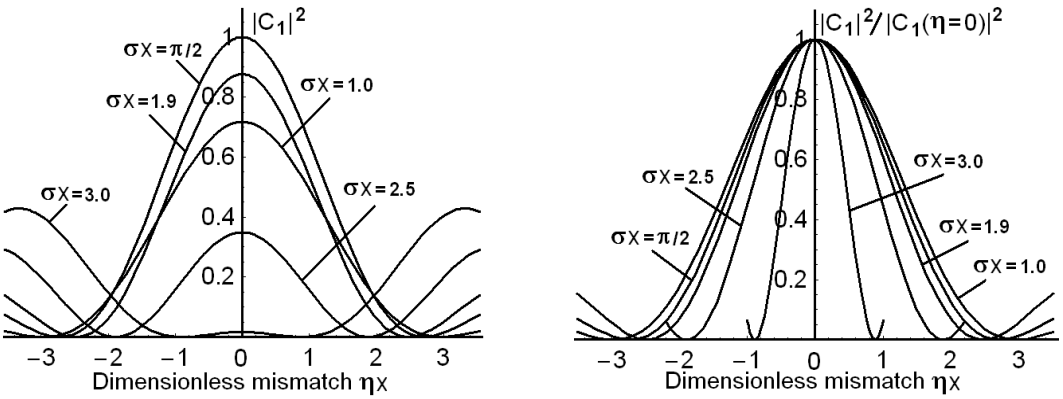

Figure 3.2. The 2D-plots $\left|\mathbf{C_1[(\sigma x),(\eta x)]}\right|^2$ for the products $\mathbf{1.0 \le \sigma x < \pi}$ with $\mathbf{q_0 / q_1 \approx 1}$: (a) for the absolute values and (b) after normalization by the zero magnitudes.

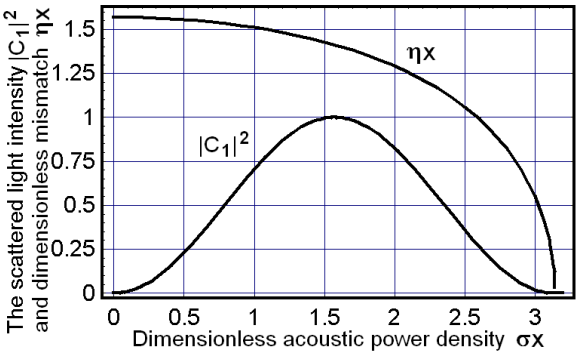

Figure 3.3. The light intensity $\left|\mathbf{C_1(x)}\right|^2$ and a one-side dimensionless mismatch $\boldsymbol{\eta x}$ versus the product $\boldsymbol{\sigma x}$.

Fig. 3.4 represent a 2D-contour plot for the normalized light intensity on the plane $\mathbf{[(\sigma x),(\eta x)]}$. The contour lies on the interval $\mathbf{0 \le \sigma x \le \pi}$ and demonstrates the tendency of squeezing the normalized light intensity profile with growing the product $\boldsymbol{\sigma x}$. As a result, one can see that profile width at $\boldsymbol{\sigma x \to \pi}$ is a few times narrower than initial one with $\boldsymbol{\sigma x \to 0}$, i.e. squeezing of the transmission function is observed.

Another set of 2D-plots for the normalized scattered light intensity $\left|\mathbf{C_1[(\sigma x),(\eta x)]}\right|^2 \cdot \left|\mathbf{C_1(\eta=0)}\right|^{-2}$ is presented in Fig.3.5 for the range of products $\boldsymbol{\pi < \sigma x < 2\pi}$. This range of products $\boldsymbol{\sigma x}$ has not been shown in Fig.3.1b. It is clearly seen from Fig. 3.5 that the profile width becomes dramatically gained within this range. The most effective case when $\left|\mathbf{C_1(\eta=0)}\right|^2 = \mathbf{1}$ is reached at $\boldsymbol{\sigma x = 3\pi/2}$, see Fig.5a, but it gives already the profile one-side width $\boldsymbol{\eta x(\sigma x = 3\pi/2) \approx 2.5}$ at the level $\mathbf{0.4053}$, which is definitely wider than the corresponding profile in the range of products $\boldsymbol{\pi < \sigma x < 2\pi}$.

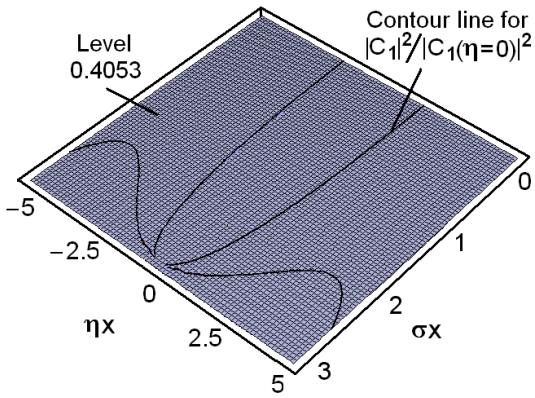

Figure 3.4. A 2D-contour for the normalized light intensity on the plane $\mathbf{[(\sigma x),(\eta x)]}$ on the interval $\mathbf{0 \le \sigma x \le \pi}$.

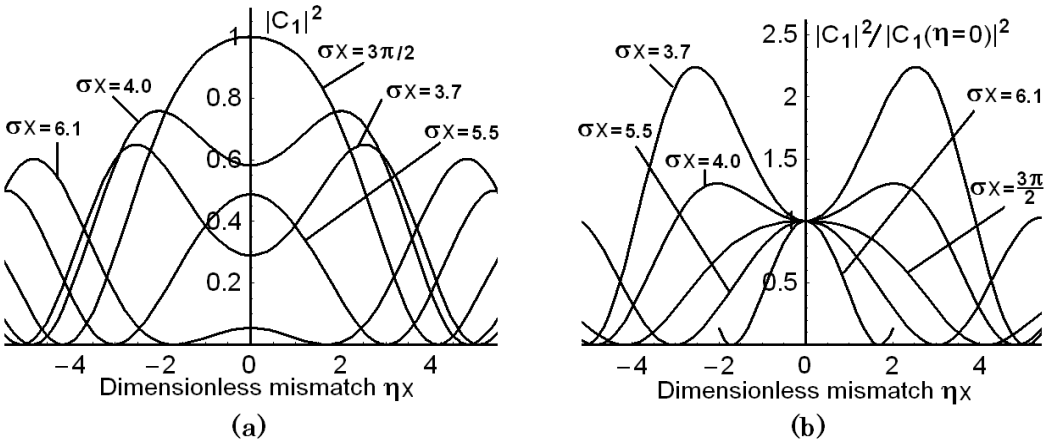

Figure 3.5. The 2D-plots $\left|\mathbf{C_1[(\sigma x),(\eta x)]}\right|^2$ for the products $\boldsymbol{\pi<\sigma x<2\pi}$ with $\boldsymbol{q_0/q_1\approx 1}$: (a) for the absolute values and (b) after normalization by the zero magnitudes.

Figure 3.6 demonstrates the general tendency to repeat squeezing the profile $\left|\mathbf{C_1[(\sigma x),(\eta x)]}\right|^2$ periodically, although only the interval $\boldsymbol{\pi\le\sigma x<3\pi}$ is depicted here. However, the presented 2D-contour plot shows clearly that each next period exhibits a wider profile in the vicinity of the points $\boldsymbol{\sigma x\to(\pi/2)+m\pi}$, $\boldsymbol{m=0,1,2,3,}\ldots$ related to maximal efficiency of light scattering as well as at the points $\boldsymbol{\sigma x\to(m+1)\pi}$ of maximal squeezing at this period with the chosen number $\mathbf{m}$. It should be noted that the dynamics of profile transformation within each particular period can be imagined in certain respects by analogy with the plots presented in Figs. 3.2 and 3.5 with obvious corrections, of course, for scaling along the $\boldsymbol{\eta x}$-axis. Thus, Fig. 3.6 makes it possible to conclude that increasing the dimensionless product $\boldsymbol{\sigma x}$ as far as the involved number $\mathbf{m}$ grows does not promise any additional squeezing the profile in comparison with the case of $\boldsymbol{m=0}$.

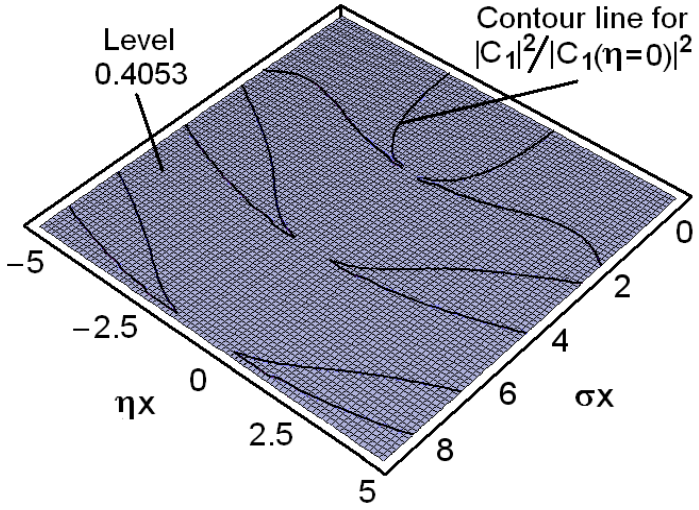

Figure 3.6. A 2D-contour plot for the normalized light intensity on the plane $\boldsymbol{[(\sigma x),(\eta x)]}$ on the interval $\boldsymbol{0\le\sigma x<3\pi}$.

3.5. Some Estimations For The $CaMoO_4$ AOTF

Together with this, one can estimate the potential contributions of the acoustic losses. The coefficient of linear attenuation for the chosen shear acoustic wave passing along the **[100]**-axis is $\Gamma = 60\,(\mathrm{dB/cm\,GHz^2})$ in a calcium molybdate single crystal [3.18]. The factor α of the amplitude acoustic losses measured in $\mathrm{cm^{-1}}$ can be expressed via the standard relation: $\alpha(\mathrm{cm^{-1}}) = 0.1152 \cdot \Gamma(\mathrm{dB/cm\,GHz^2}) \cdot f^2(\mathrm{GHz})$. The carrier frequency f_0, peculiar to the collinear acousto-optical interaction in calcium molybdate at the above-mentioned light wavelength $671\,\mathrm{nm}$, can be calculated as $f_0 = \Delta n \cdot V/\lambda \approx 37.3\,\mathrm{MHz}$, so that one can estimate the amplitude factor of acoustic losses by $\gamma = \Gamma(\mathrm{dB/cm\,GHz^2}) \cdot f_0^2(\mathrm{GHz}) \approx 0.08334\,(\mathrm{dB/cm})$ and $\alpha = 0.00962\,\mathrm{cm^{-1}}$. Due to the smallness of the factors γ and α, one can neglect the effect of acoustic attenuation and consider this case like practically lossless one.

The angular divergence of acoustic beam in a calcium molybdate collinear cell at the frequency $f = 37.3\,\mathrm{MHz}$ can be estimated as well. Practically, a reliable spatial size of the initial acoustic beam aperture that is considered is close to $d \approx 0.2$ cm. Thus, one can estimate $\Lambda = V/f = 7.91 \cdot 10^{-3}\,\mathrm{cm}$, and $\varphi = \Lambda/d \approx 3.955 \cdot 10^{-2}\,\mathrm{rad} \approx 2.267^{0}$, and conclude that the angular divergence of acoustic beam can be also omitted. The full mismatch $\Delta\eta$ is connected with the frequency resolution δf. Due to the above-mentioned expression $\Delta\eta = \pi\,\delta f/V$, one can find $\delta f = (\Delta\eta \cdot x)V/(\pi L)$.

At this step, a few practical numerical estimations inherent in the collinear interaction at the light wavelength of $\lambda = 671\,\mathrm{nm}$ in the $CaMoO_4$-crystalline cell with $M_2 \approx 1.977 \cdot 10^{-18}\,(\mathrm{s^3/g})$ and $L = 4.4\,\mathrm{cm}$ are ready to be performed. The periodicity of collapsing the resolution (see Fig. 3.7) is characterized by simple formula $\sigma_m L = m\pi$, so that for a pair of the first periods with $m = 1, 2$ one has $\sigma_1 = \pi/L \approx 0.714\,\mathrm{cm^{-1}}$ and $\sigma_2 = 2\pi/L \approx 1.428\,\mathrm{cm^{-1}}$.

Using the standard determination introduced above, one can write

$$\text{a)}\ \ \sigma = U_0\sqrt{q_0 q_1} \approx \frac{\pi}{\lambda}\sqrt{\frac{P}{2}M_2}\ , \qquad \text{b)}\ \ P \approx \frac{2\lambda^2\sigma^2}{\pi^2 M_2}\ . \tag{3.20}$$

Consequently, Eq.(3.20) gives $P\,[\mathrm{W/mm^2}] \approx 0.457 \cdot \left(\sigma\,[\mathrm{cm^{-1}}]\right)^2$, so that $P_1 \approx 0.233\,[\mathrm{W/mm^2}]$ for σ_1 and $P_2 \approx 0.932\,[\mathrm{W/mm^2}]$ for σ_2, see Fig. 3.7. One can see that reaching the second point of collapsing the resolution needs four-times higher acoustic power density in comparison with the first point and looks rather conjectural from the viewpoint of requirements to electric strength inherent in the available piezoelectric transducer. Then, the above-presented theoretical 2D-contour plot had shown that each next period

exhibits a wider profile in the vicinity of the points $\sigma x \to (\pi/2)+m\pi$, $m=0,1,2,3,\ldots$ related to maximal efficiency of light scattering at this period.

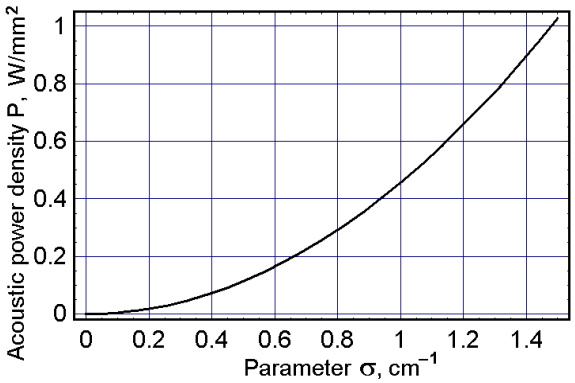

Figure 3.7. Acoustic power density P vs. the parameter σ at $\lambda = 671\,nm$ in the above-chosen collinear $CaMoO_4$-crystalline cell.

3.6. Scheme for the experiments with a $CaMoO_4$ cell

To realize experimentally the process of filtering the schematic shown in Fig. 3.8 is used, It consists of a continuous-wave laser, a $CaMoO_4$-crystalline acousto-optical cell with a pair of the Glan-Thompson crystalline polarizers (with the extinction ratio 10^5 each) whose combined layout is presented in details in Fig. 3.9, a silicon photo-detector, and a set of electronic equipment for both generating and registering the corresponding electric ultra-high-frequency (UHF) radio-wave signals. Initially, the tunable UHF-signal is applied to the electronic input port of the collinear acousto-optical cell through a wide-band UHF-amplifier HD18858 ($10-1000\,MHz$, $8\,W$), see Figs. 3.8 and 3.9, and to the input of an oscilloscope (or computer) as the etalon signal, see Fig. 3.8.

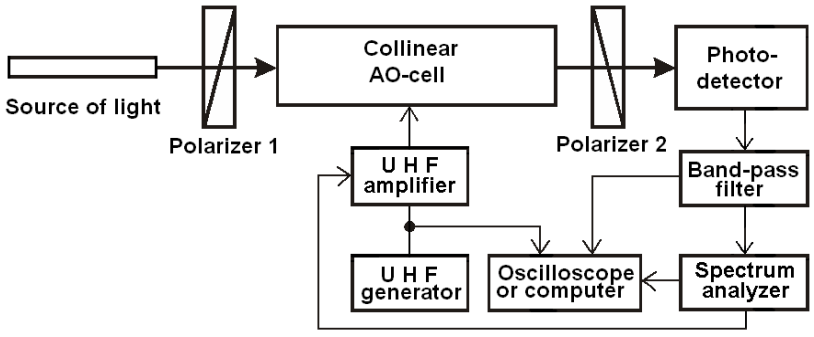

Figure 3.8. Schematic arrangement of the experimental set-up

A two-mode co-propagating collinear $CaMoO_4$ crystalline cell was characterized by a crystal length $L = 4.4\,cm$ along the $[100]$-axis, an acoustic velocity $V = 2.95 \cdot 10^5\,cm/s$ for the shear elastic mode whose displacement vector is oriented along the $[001]$-axis. The continuous-wave beam at a dark-

red light wavelength of $\lambda = 671\,\text{nm}$ (the output optical power $\sim 40\,\text{mW}$) had been chosen, first, to minimize the controlling acoustic wave frequency down to about $35\,\text{MHz}$ in a view of realizing as close as possible "almost lossless" regime for the propagation of acoustic beam through the $CaMoO_4$ crystalline cell and, second, to keeping just the visible range of operation with light beams simplifying the experimental conditions of observations. Thus, the light beam at $\lambda = 671\,\text{nm}$ with the output optical power $\sim 40\,\text{mW}$ was used as an optical pump during the experiments providing the traveling-wave regime of interaction between the pumping light beam and the acoustic wave. The first polarizer was precisely aligned in correspondence with the optical axes of a crystal in a cell. As the optical pump and the continuous-wave acoustic wave were interacted, already two orthogonally polarized light beams, incident and signal ones, passed through a cell. The second polarizer gave us an opportunity to be aligned in correspondence with the polarization of the signal beam and to extract the output optical signal, see Fig. 3.9.

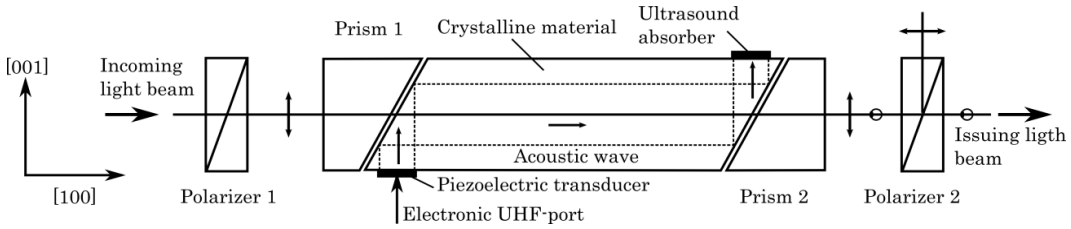

Figure 3.9. Scheme of the co-propagating collinear $CaMoO_4$-cell providing the traveling-wave regime of interaction between the pumping light beam and the continuous-wave lossless acoustic beam.

Then, one can restrict oneself by a maximal level $P \le 0.5\,\text{W/mm}^2$ of acoustic power density, which is conditioned by the absolute acoustic power magnitude of about $2\,\text{W}$ and the acoustic beam cross section of about $4\,\text{mm}^2$ in the chosen collinear acousto-optical cell. Consequently, one can calculate that $\sigma \le 2\,\text{cm}^{-1}$. These estimations demonstrate that the above-noted limitations on both the needed acoustic power density $P_1 \approx 0.233\,\text{W/mm}^2$ and the parameter $\sigma_1 \approx 0.714\,\text{cm}^{-1}$ lie in the frames of accessible value, while similar parameters P_2 and σ_2 for the second point of collapsing the resolution are beyond these frames.

The nonlinear dynamics of varying the transition functions of the optical filter under consideration has been sequentially followed during the experiments as the acoustic power density of the finite amplitude grows. A few examples of the corresponding digitized oscilloscope traces are shown in Fig. 3.10 [3.19]

Now, let us discuss this set of oscilloscope traces for the scattered light component intensity $|C_1|^2$ detected during the experiments with the collinear $CaMoO_4$ crystalline cell and estimated at the level 0.4055 conditioned by the Rayleigh criterion. All these traces can be easily interpreted in terms of the

above-developed theory taking into account that. The first trace in Fig. 3.10a reflects the filter transition function inherent in almost the regime with infinitely small amplitude of the controlling acoustic signal due to the dimensionless value $\sigma L = 0.21$ is very close to zero. This value (which is non-zero, in fact) had been taken as an example to show rather adequately conventional representation for the transition function width or, what is the same, the filter frequency resolution, being close to $\delta f \approx V/L \approx 68.44\,\text{kHz}$, as well as to have a chance for identifying the output response whose relative intensity is small enough, i.e. even less then $5\,\%$. The second and third traces, peculiar to $\sigma L \approx 1.0$ and $\sigma L \approx \pi/2$ are presented in Figs. 3.10b and 3.10c, respectively.

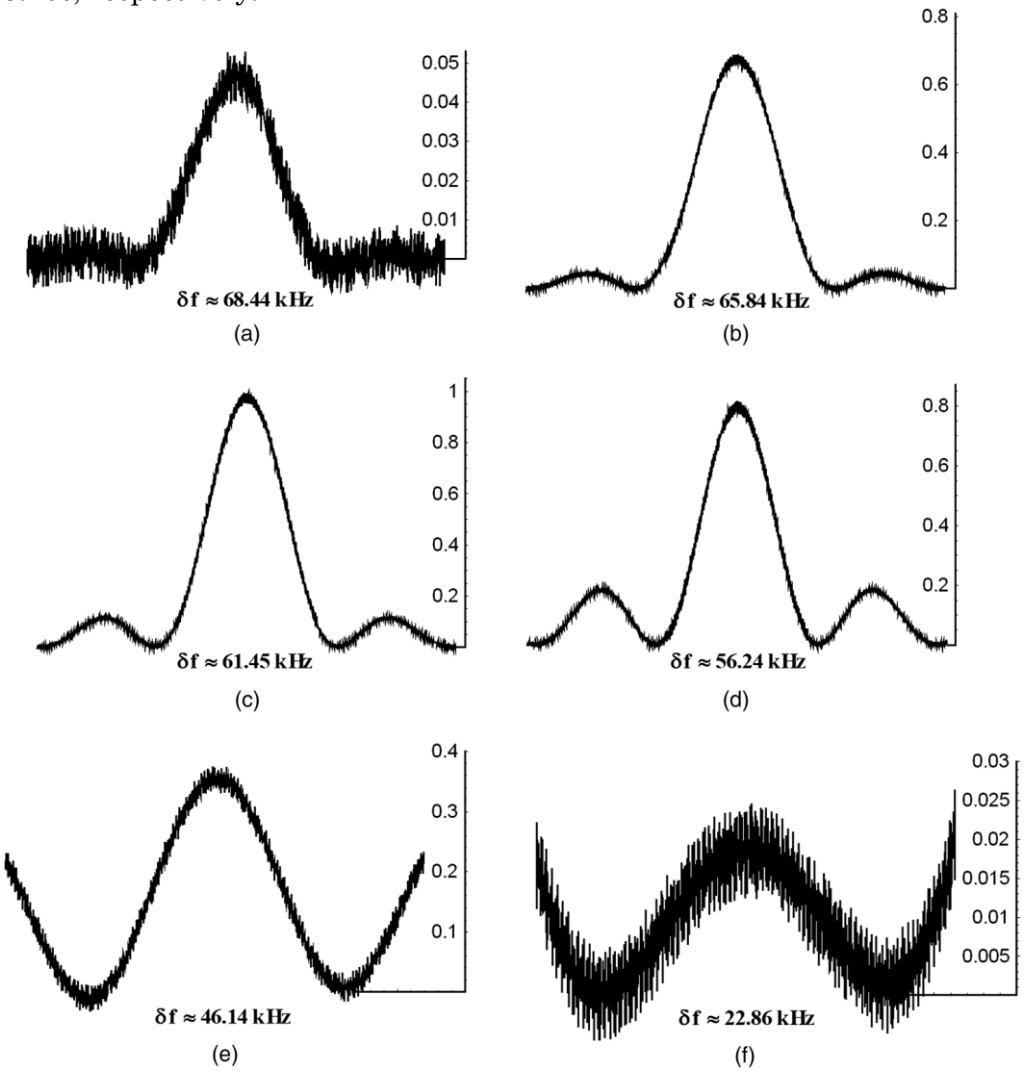

Figure 3.10 The digitized oscilloscope traces for the scattered light intensity $|C_1|^2$ observed at the output of the collinear $CaMoO_4$ cell at the carrier acoustic frequency of $\sim 37.3\,\text{MHz}$ and estimated at the level 0.4055. Reshaping the transmission function is followed at the same optical pump in variable scales: (a) $\sigma L = 0.21$, $P \approx 0.00104\,[\text{W/mm}^2]$; (b) $\sigma L \approx 1.0$, $P \approx 0.0236\,[\text{W/mm}^2]$; (c) $\sigma L \approx \pi/2$, $P \approx 0.0582\,[\text{W/mm}^2]$; (d) $\sigma L \approx 2.0$, $P \approx 0.0944\,[\text{W/mm}^2]$; (e) $\sigma L \approx 2.5$, $P \approx 0.148\,[\text{W/mm}^2]$, and (f) $\sigma L \approx 3.0$, $P \approx 0.223\,[\text{W/mm}^2]$.

From a viewpoint of widely used acousto-optic approach, they can be considered as a natural testimony of growing the relative intensity of the output optical signal up to 0.715 and ~ 1.0 under action of the increasing acoustic power density. They both exhibit the optical resolution of more or less the same order, which varies slightly from the above-mentioned $68.44\,\text{kHz}$ to $\delta f \approx 65.84\,\text{kHz}$ and $\delta f \approx 61.45\,\text{kHz}$, respectively. Such a conclusion looks rather plausible within quasi-linear approximation for the transition function as well as in the course of possible measurements in the frequency domain with not enough accuracy. Nevertheless, further increase of the acoustic power density, depicted by the traces with $\sigma L \approx 2.0$ and $\sigma L \approx 2.5$ in Figs. 3.10d and 3.10e, is able to demonstrate step by step that the existing specific acousto-optical nonlinearity leads to squeezing the transition function or to improving the frequency resolution to $\delta f \approx 56.24\,\text{kHz}$ and $\delta f \approx 46.14\,\text{kHz}$, respectively. This process is accompanied by decreasing the relative intensity of the output optical beam down to about 0.82 and 0.35 in the so chosen points. Finally, the last trace, see Fig. 3.10f, illustrates obviously nonlinear process of squeezing the transition function or improving the frequency resolution in the vicinity of the first point $\sigma L = \pi$ of a collapse. Namely the value $\sigma L \approx 3.0$ has been taken to have an opportunity for revealing the transition function characterized by $\delta f \approx 22.86\,\text{kHz}$ whose relative intensity becomes already dramatically small and does not exceed $2\,\%$.

3.7. Conclusions

It was revealed the nonlinear squeezing of the transition function inherent in the collinear acousto-optical interaction under condition of the simplifying approximation of lossless (or low-loss) propagation for the acoustic waves. This nonlinear effect can be interpreted also as improving the spectral and frequency resolution peculiar to the collinear acousto-optical filter operated by the controlling acoustic waves of the finite amplitude. Rather adequate theory of this effect has been developed analytically and illustrated via the corresponding computer simulations. In particular, a periodicity for the nonlinear squeezing of the transition function, which includes a set of points for its collapses originating periodically, has been found and estimated. It has been shown that the first period of similar collapsing exhibits the best relation between the width and magnitude of the squeezed transition function from the viewpoint of practical application. Then, the needed estimations has been performed for the collinear interaction, which made it possible to choose a dark-red light laser beam, lying still in the visible range, and a low-frequency acoustic wave, providing its almost lossless propagation, in a $CaMoO_4$ single crystal. Finally, the results of the experiments illustrating the nonlinear squeezing of the transition function with lossless propagation of acoustic waves in the collinear calcium molybdate crystalline cell have been presented and briefly discussed.

Chapter 4

Acousto-Optical Triple Product Processor for Astrophysical Applications

The spectroscopy is a very important technique for the study of the radiation, focused on astrophysical application, the use of acousto-optical phenomena is widely used all around the world. A Triple Product Processor (TPP) was developed in the 70s for signal processing and spectroscopy applications. In this chapter a new setup for the TPP for $3-$ inch optics is proposed. It is described and analyzed theoretically, first by describing the basic theory needed for its study, then the fundamental concepts of the operation of a TPP focused on the time integration analysis, and later the schematic arrangement proposed along with some estimations of the potential performance for such a device.

4.1. Introduction

An extremely adaptable optical architecture of an acousto-optical triple-product processor, which had been initially suggested in Ref.[4.1, 4.2] and whose general schematic arrangement is presented in Fig.4.1, will be discussed.

The laser diode or LED, for example, can be used as a point light source whose radiation is modulated in time by the initial electronic signal $\Phi_0(t)$. The vertically oriented acousto-optic cell AOC-1 realizes a modulation by the first additional electronic signal $\Phi_1(t)$. This cell is lighted by the optical beam from a point source through the spherical lens $L1$ and the cylindrical lens $L2$. The light beam, scattered by the AOC-1, is modulated by the product $\Phi_0(t)\cdot\Phi_1(t-x_1/V_1)$. In a view of lighting the AOC-2, which is placed

horizontally, the output light beam after the AOC-1 is broadened horizontally and focused vertically by the spherical lens **L3**. Let the second additional electronic signal, which is applied to the AOC-2, is $\Phi_2(t)$. As a result, the light beam, scattered by the AOC-1, is modulated by the product $\Phi_0(t)\cdot\Phi_1(t-x_1/V_1)\cdot\Phi_2(t-x_2/V_2)$.

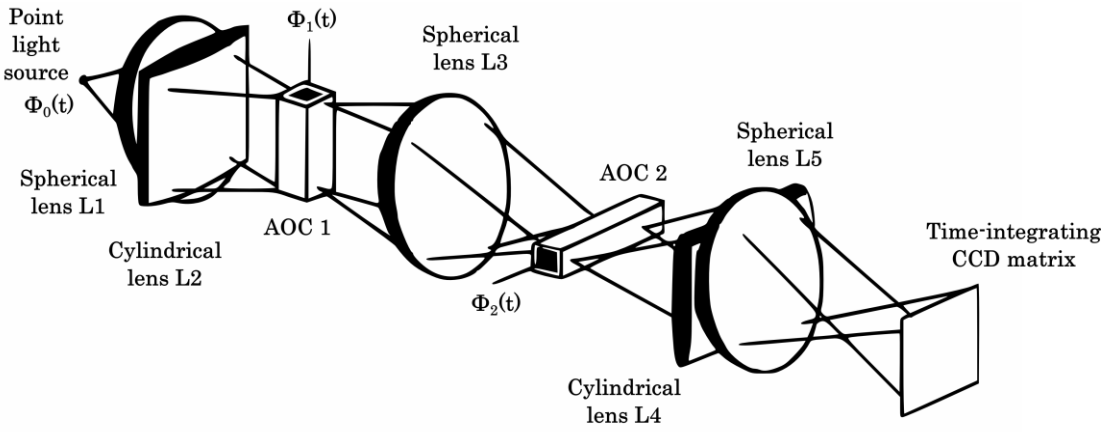

Figure 4.1. General schematic arrangement of optical components for a triple-product acousto-optical processor.

The obtained product includes in fact two time delays $t_1 = x_1/V_1$ and $t_2 = x_2/V_2$, where $x_{1,2}$ and $V_{1,2}$ are physical spatial coordinates along the corresponding acousto-optical cells and the acoustic wave velocities, respectively. These time delays t_1 and t_2 must satisfy the inequality $0 < (t_1, t_2) < T$, where the aperture transit time T of the modern acousto-optical cells can be equal to about $10-50\,\mu s$. The cylindrical lens **L4** and the spherical lens **L5** shape the image of the AOC-2 at the output plane in horizontal direction, while the spherical lenses **L3** and **L5** give the image of the AOC-1 at the output plane in vertical direction. A two-dimensional matrix of photo-detectors is placed in the output plane, so that charges $g(t_1, t_2)$ collected by each individual pixel under acting the light during the time T_i at a point (x,t) are proportional to

$$g(t_1, t_2) = \int_{T_i} \Phi_0(t)\ \Phi_1(t - x_1/V_1)\ \Phi_2(t - x_2/V_2)\, dt, \qquad (4.1)$$

where T_i is the time of integration, which is limited by the detector and could be about $1\,ms$ or more; the time delays t_1 and t_2 represent a pair of the coordinates in the output focal plane, i.e. in a plane of the CCD matrix photo-detector. Such a system represents a triple-product processor. This processor consists of a pair of the two one-dimensional correlators operating simultaneously in two mutually orthogonal planes. However, the system does not simply collect two one-dimensional conversions; the final result appears within a joint two-dimensional processing of all the input signals. This architecture always calculates Eq.(4.1), but it exhibits really high flexibility,

because all the three input signals are given initially as electronic signals, so that this processor can be easily re-oriented from fulfilling one algorithm to another in the frames of completely the same optical resources simply by varying the input electronic signals $\Phi_j(t)$ with $(j=0,1,2)$.

In figure 4.2 are shown the both main parts of the processor. The one related to the space-integrating processing made using the first cell (oriented to the coarse resolution) and the time-integrating processor made with the second cell (oriented to the fine resolution) and the photo detector matrix.

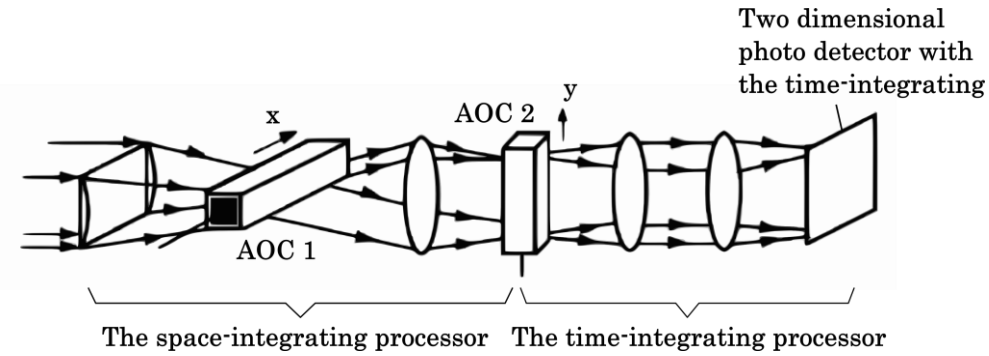

Figure 4.2 Schematic arrangement of TPP showing space and time integration.

4.2. Time Integration

The use of time integration technique in acousto-optics data from 1970 with the work of Montgomery [4.3] and later studied by several researchers; Turpin, Sprage, Bader, and Kellman just to mention some of them.

4.2.1.Time Integrating Correlation

The simplest case of time integrating processor is the time integrating correlator [4.2], Fig. 4.3. In this correlator, the first Bragg cell is modulating the intensity of the laser beam with the signal $f(t)$. Then, the diffracted light cross the second Bragg cell which modulates the intensity of light again but with the signal $g(t-x/V)$, here, x is the position along the Bragg cell and V still stands for the speed of acoustic wave in the cell. So, the output signal in the detector at the x position is:

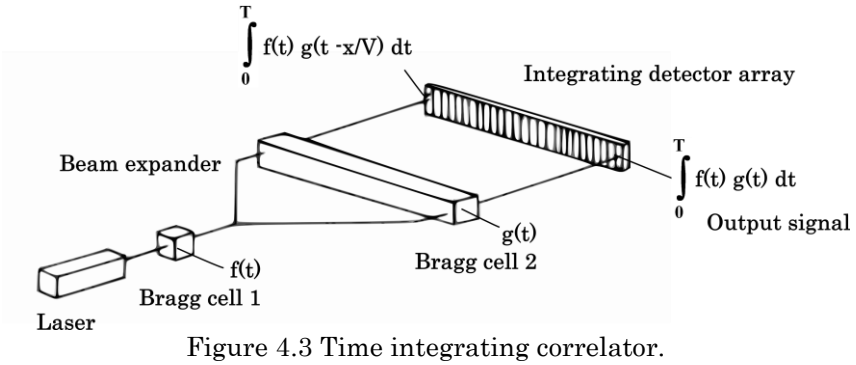

Figure 4.3 Time integrating correlator.

$$r(x) = \int_0^T f(t)\, g(t - x/V)\, dt \,, \tag{4.2}$$

T is the integration time of the detector, with the selected detector, this can range from $38\,\mu s$ to $60\,s$. Note that, according to the sampling theorem, the Bragg cell bandwidth must be twice the bandwidth of the signals of interest.

4.2.2.Resolution of Spectral Analysis

To estimate the resolution it is necessary to introduce some characteristic parameters in the frequency analysis. The first is the number of resolvable spots, which is given by [4.4]:

$$N = \tau \Delta f = TB \,, \tag{4.3}$$

where $\tau = D/V$ is the transit time of the signal through the acousto-optical aperture D of the device, V is the acoustic wave velocity, Δf is the bandwidth of the acousto-optical cell. So, the number of resolvable spots is equal to the time-bandwidth product.

Now, chirp signals must be introduced in the acousto-optical cells to make the spectrum analysis. The chirp rate $a = \Delta f / \tau$, called the fast chirp rate will be injected on the first cell. With this, one will obtain the coarse frequency resolution. The second cell will be controlled by a slow chirp signal with a chirp rate b, having $b = a/N$. This slow chirp determines the fine frequency resolution $f_0 = 1/T_s$, where T_s is the duration of the slow chirp [4.5].

4.3. Rayleigh Criterion and Sampling Theorem

4.3.1.Practical Estimations

In order to get the best performance of the TPP, will be needed the largest number of spots which the CCD pixel array would resolve. To estimate this, will be taken into account the sampling theorem and the spot size of the last lens in the TPP setup.

The sampling theorem states that [4.6]:

"If a function contains no frequencies higher than $W\,Hz$, it is completely determined by giving its ordinates at a series of points spaced $1/2W$ seconds apart."

Translating this to space coordinates it means that if one have one signal of size $X\,meters$ (space frequency would be $(1/X)\,m^{-1}$) will be completely determined if samples are taken every $(X/2)\,m$. For example; with a spot size of $10\,\mu m$, according with the sampling theorem, taking measurements every $5\,\mu m$ would be enough to recover the signal and, at the same time, avoid oversampling.

It is known from the literature [4.7] that the amplitude of a Gaussian beam have the form:

$$\psi_0 = \exp\left[-\frac{r^2}{\omega(z)^2}\right], \tag{4.4}$$

Where r is the radius from the center, having its maximum at $r = 0$.

$$\omega(z)^2 = \omega_0^2\left[1 + \left(\frac{z}{z_0}\right)^2\right] \tag{4.5}$$

is a function related to the width of the beam, this function will be changing as the beam propagates through the z direction. z_0 is a measure of the length where the beam width will have almost a constant value. ω_0 is the minimum width of the beam and it is called the "spot size". When the radius of the beam is equal to this spot size, the amplitude of the beam will be e^{-1} and the intensity, which is proportional to the amplitude squared, will be e^{-2}. This will be called the e^{-2} level.
A focused Gaussian beam will have a minimum waist,

$$\omega_0 \approx \lambda f^{\#} = \frac{\lambda F}{D}, \tag{4.6}$$

where $f^{\#}$ equals focal length (F) divided by the diameter (D) of the lens. With this limitation the smallest spot size for the lenses in the market will be around $7\mu m$. Besides of that, the aberrations of the lens should be taken into account, which will enlarge even more the size of the spot. For that reason, the analysis of the spot sizes of several lenses should be done in order to select the one which will perform better in the $3-$ inch TPP.

Now there is another problem, the reduced number of large high quality lenses in the market. Several catalogs were checked and the lenses chosen for the analysis were the AC508-500-A from Thorlabs, a $2-$ inch lens with a focal length of $500mm$, and the #30-976 from Edmund Optics, a $3-$ inch lens with a focal legth of $849.9mm$, both of them are achromatic lenses and designed for $\lambda = 587.6nm$.

The analysis was made using the software OSLO (Optics Software for Layout and Optimization) from Lambda Research Corporation. In the software the properties of the lens must be specified; the radius of curvature of each surface, thickness, material, and the aperture radius.

After that, the properties of the beam must be provided but, before this, the criterion of the size beam must be established. The previously estimated spot size was calculated at the level of e^{-2} but, according to the Rayleigh Criterion [4.5], one just need the spot size at the level of 0.405, see Fig. 4.4. So, the spot size must be recalculated to this level. To do this, the Gaussian distribution was adopted for the beam profile. The ratio of the spot size at the level of e^{-2} divided by the spot size at the level of 0.405 was calculated as, approximately,

3/2, see Fig. 4.5. With this in mind, instead of using a Gaussian beam with $\omega_0 = 3''$, a waist of $\omega_0 = 4.5''$ will be selected. While introducing these parameters in OSLO, one must be very careful because the software works with radius instead of the diameters.

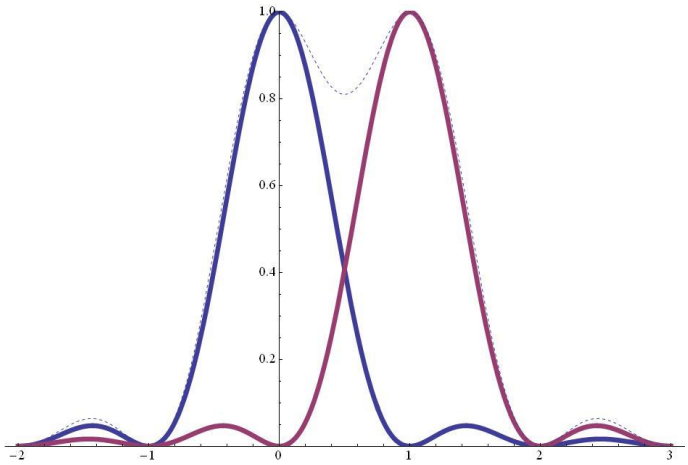

Figure 4.4. Rayleigh Criterion for resolving two signals. The dashed line is the sum of the intensities of the two signals.

First the parameters of the Gaussian beam must be established by clicking "SETUP" on the "Surface Data Spreadsheet", enabling the "Gaussian beam" option and selecting the beam size (at the level of $\mathbf{e^{-2}}$). For this analysis a radius of **57.15mm** (for the **3''** lens) and **38.1mm** (for the **2''** lens) were selected in order to have the beam at the level of **0.405** on the edges of the lenses. Now it is time to do the analysis using the "Truncated Gaussian Beam…" feature in OSLO. Then, the monochromatic option is selected and using **64** points for better resolution. The results show us spot sizes of **9.6μm** for the Thorlabs lens, Fig. 4.6a, and **11.6μm** for the Edmund Optics lens, Fig. 4.6b. Both results at the level of $\mathbf{e^{-2}}$, using the approximation for the **0.405** level, the sizes would be **6.4μm** and **7.7μm**, respectively.

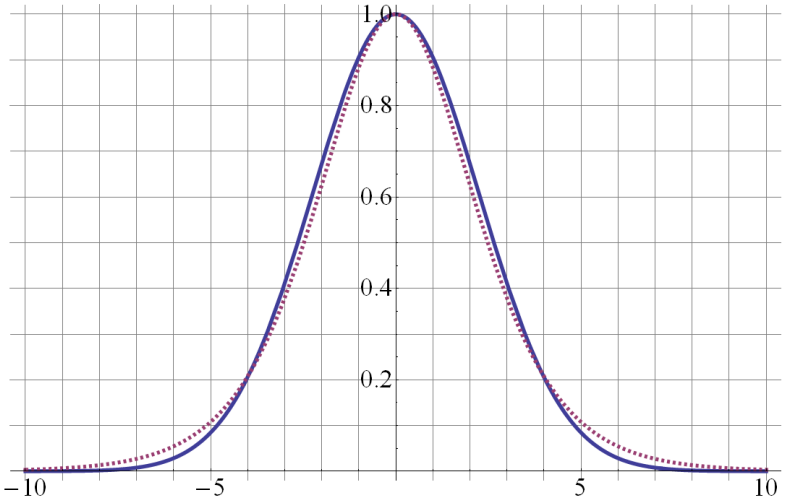

Figure 4.5. Gaussian Distribution function (continuous) and $\mathbf{Sinc^2}$ function (dashed).

a.

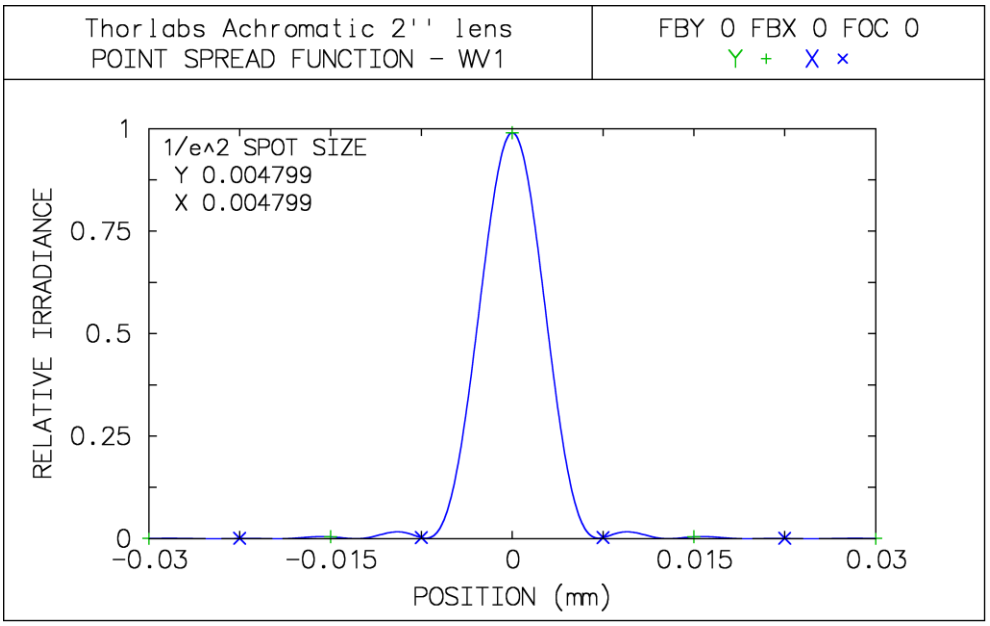

b.

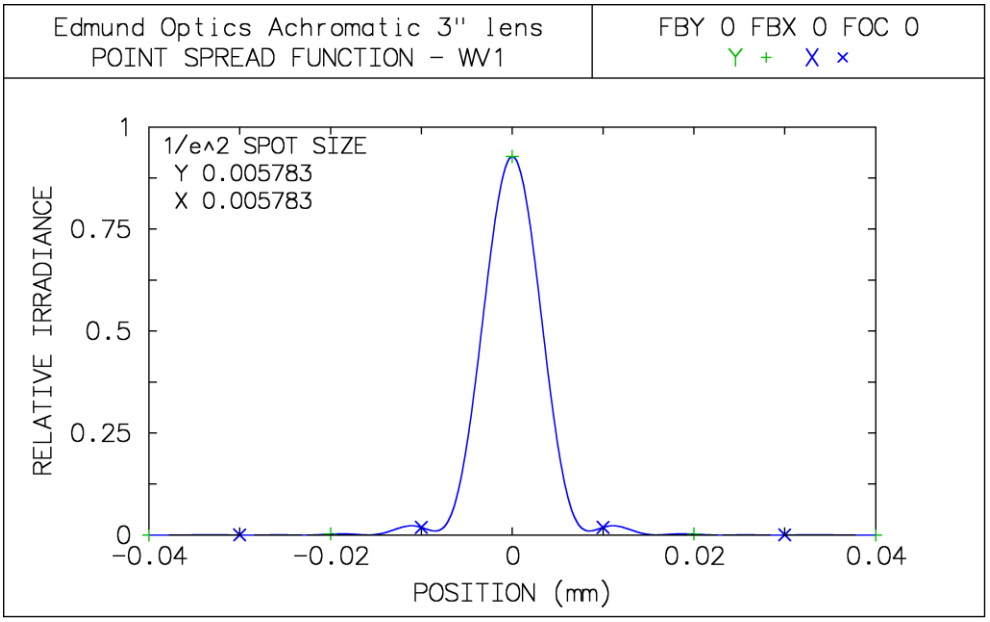

Figure 4.6. OSLO Point Spread Functions for: a) Thorlabs AC508-500-A lens and b) Edmund Optics #30-976 lens

4.3.2. CCD Selection Requirements

First, the choice between CCD or CMOS sensors has to be taken. The main advantage of a CCD over a CMOS is the higher dynamic range, moreover the CCD have less noise, making it ideal for low-light imaging. The CCD also have a more uniform shuttering which is better for imaging objects in motion. With the estimated spot sizes one is ready to look for a CCD camera with a pixel size of half the spot size generated by the last lens to be in agreement with the sampling theorem. The most common pixel size in the optics specialized market is about **4.65 µm** for a **1280×1024** CCD array which would

not be small enough for the needs of this problem. There is also CCD arrays with a pixel size of $3.45\mu m$ in a matrix of 2448×2050 from Edmund Optics, model number EO-5023M, which would be more suitable for this prototype. The complete characteristics of EO-5023M are shown in Table 4.1

Table 4.1 Characteristics of EO-5023M

Type of Sensor	Sony ICX655
Sensing Area, H x V (mm)	8.45 x 7.07
Imaging Device	Progressive Scan CCD
Pixels (H x V)	2448 x 2050
Pixel Size, H x V (µm)	3.45 x 3.45
Pixel Depth	12-bit
Frame Rate (fps)	6
Exposure time	38µs – 60s
Dimensions (mm)	34 x 32 x 34.4

4.4. Optical Arrangement of Triple Product Processor

Here is depicted, Fig 4.7, the proposed experimental arrangement for the TPP for $3-$ inch optics. The distances of the picture are explained in the subsection 4.3.2 and gathered it Table 4.2.

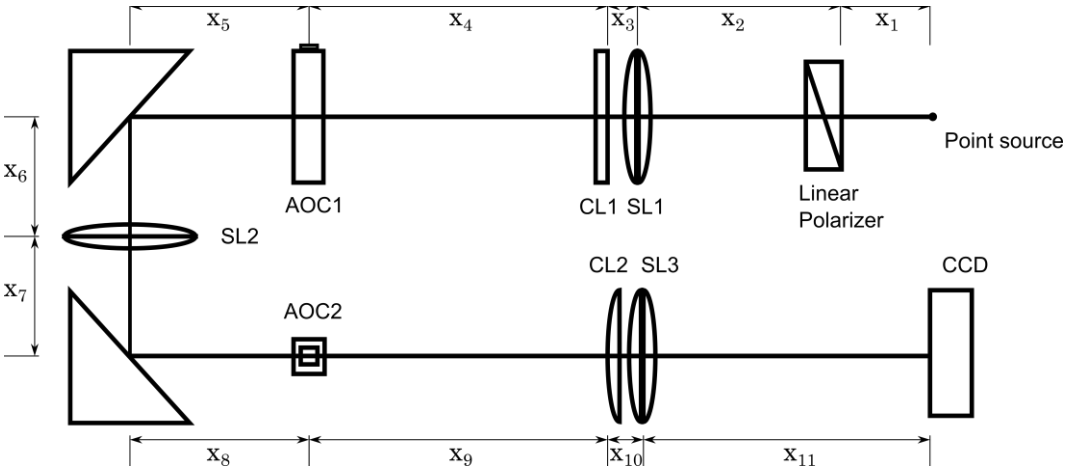

Figure 4.7 Layout of the TPP, SL is for the spherical lenses, CL cylindrical lenses, 2 acousto-optical cells (AOC).

4.4.1. Experimental Setup

The arrangement starts with a solid state laser, for the maximum input power, coming out from an optical fiber which will work as a point source. Then a Glan-Thompson polarizer is used to ensure the polarization of the

light. Then a spherical lens (SL1) will collimate the light before it passes through the first cylindrical lens, which will focus the light in a line over the first acousto-optical cell (AOC1). At the same effective distance of the CL1 and AOC1 will be a second spherical lens (SL2 with the same focal distance of CL1) which will collimate the beam along on axis and focus it on the perpendicular axis. Now the light will be focus on a line over the second acousto-optical cell (AOC2 perpendicular to AOC1). Then the light will be collimated again with the second cylindrical lens (CL2) before it reaches the last spherical lens (SL3) which will collect all the light and focus it on the CCD camera.

4.4.2. Components Selection

Here is the complete list of components needed and the motivation for its selection among several options in the market.

Solid State Laser

First of all, Diode Pumped Solid State (DPSS) laser was selected over other kinds of laser because its high output power and faster speed of operation besides the option of a fiber coupled output. The selected DPSS laser is Cobolt Samba from the Swedish company Cobolt, with $\lambda = 532.1\,\text{nm} \pm 0.3$ and a CW output power of $300\,\text{mW}$. Coupled to a single mode optical fiber with a core diameter of $3.5\,\mu\text{m}$. Because of diffraction effect the beam will be spread in to an angle of $\theta_0 = 2\lambda/\pi\omega_0 \approx 11°$ [4.7] at the level of e^{-2} in intensity.

Polarizer

A Glann-Thompson polarizer was selected because of its high extinction ratio against other kinds of polarizers. GTH10M-A from Thorlabs was selected, with an extinction ratio of $100{,}000:1$ and antireflection coating for $350-700\,\text{nm}$. Due to the angle of the expanding beam and the longitude of the polarizer, the polarizer must be at around $10\,\text{mm}$ from the point source, then, $x_1 = 10\,\text{mm}$.

First Spherical lens

The first lens must be located at its focal distance from the point source in order to collimate the light. The criteria for selecting the focal distance of this lens is to have the lens completely illuminated by the point source at the level of 0.405. Using the angle θ_0, previously calculated, the minimum distance would be

$$x_{min} = 1.5\,\text{inches}/\tan(\theta_0/2) = 39.57\,\text{cm}$$

at e^{-2} level, which for the level of 0.405 would be $x_{min} \approx 60\,\text{cm}$. So the previously analyzed lens from Edmund Optics #30-976 would be in accordance with this limit. $x_2 = 849.9\,\text{mm} - x_1 = 839.9\,\text{mm}$.

Cylindrical lenses
For $3-$ inch optics there are not too many options in the catalogs. The best option available was the cylindrical lens LJ1267L1-A from Thorlabs, with a focal length of $250\,mm$ and size of $62\,mm \times 60\,mm$, whose diagonal is about $86\,mm$. Here, the spherical and cylindrical lenses are separated $20\,mm$ in order to give some space between the mounts. $x_3 = x_{10} = 20\,mm$, note that these distances are between the focal planes of the lenses. $x_4 = 250\,mm$.

Acousto-Optical Cells
Based on previous studies [4.8]the selected material for the AO cells is TeO_2 which will give us 4000 resolvable spots for the $60\,mm$ aperture and a working frequency around $50\,MHz$.

Mirrors
In order to reduce the size of the experimental arrangement, one needs to use a set of mirrors. The selected mirrors are 2 Edmund Optics #47307, a $75\,mm$ right angle mirror with enhanced aluminum coating.

Second Spherical lens
The second spherical lens is used to collimate the light coming from the first AOC on one axis while focusing it on the other, perpendicular, axis. To do so, this lens need to have the same focal length as the cylindrical lens: $250\,mm$. The total length between the AOCs and the collimating/focusing lenses, must be the same, $x_5 = x_8 = 150\,mm$, $x_6 = x_7 = 100\,mm$, and $x_8 = 250\,mm$.

Third Spherical lens
Based on the analysis made in the section 4.1, the achromatic lens #30-976 from Edmund Optics with a focal length of $849.9\,mm$ and $3-$ inch diameter was selected, with an estimated spot size of $7.7\,\mu m$. $x_{11} = 849.9\,mm$.

CCD camera
As mentioned in subsection 4.1.2, the best option for the selected last lens in the arrangement is the $5\,Megapixel$ CCD camera EO-5023M from Edmund Optics with a pixel size of $3.45\,\mu m$. According to the sampling theorem at least 2 detector elements per spot, condition fully satisfied with the $3.45\,\mu m$ pixels for the $7.7\,\mu m$ spot.

Mounts
To ensure the maximum stability and the precision for the alignment of the experimental arrangement solid mounts with five degrees of freedom are required (3 translational and 2 rotational), each one with micrometric precision, for every single component. A third rotational degree of freedom is added for the AO cells.

Table 4..2 Distances for the layout of TPP, Fig 4.6, the values are on millimeters.

x_1	x_2	x_3	x_4	x_5	x_6	x_7	x_8	x_9	x_{10}	x_{11}	Total
10	839.9	20	250	150	100	100	150	250	20	849.9	2739.8

All the selected components are depicted in Fig. 4.8 following the layout proposed in Fig. 4.7

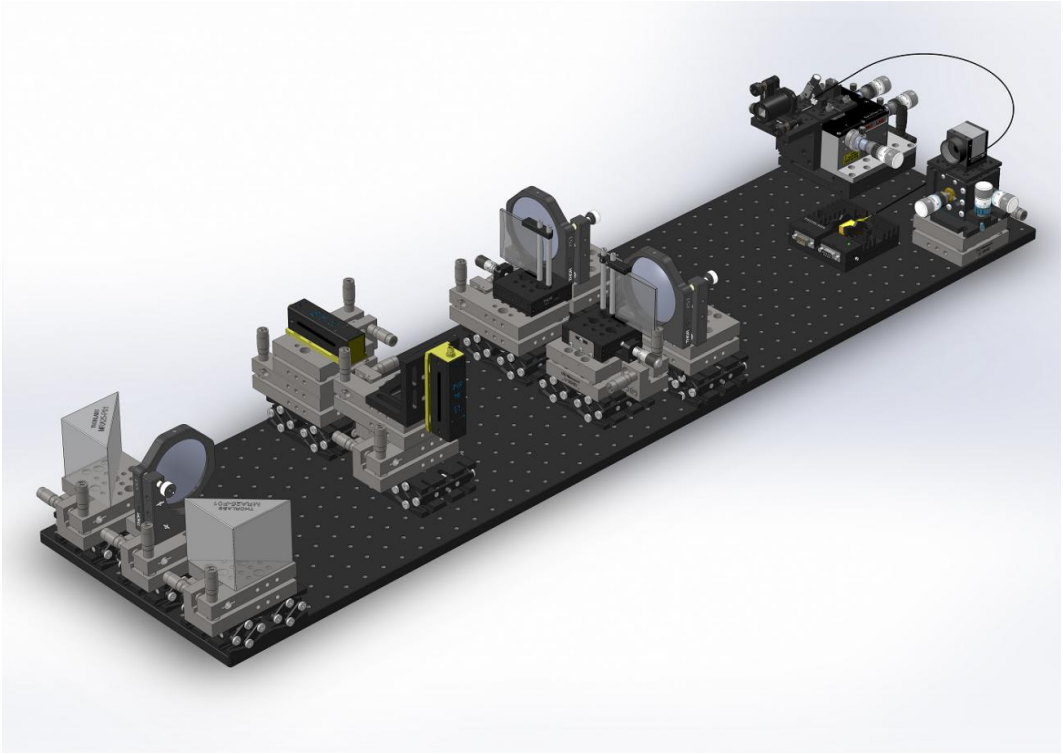

Figure 4.8. Experimental setup with the selected components.

4.5. Some estimations

From previous studies [4.8], the time-bandwidth of an acousto-optical cell made of TeO_2, with a velocity of $0.65\times10^5\ cm/s$, an effective aperture of 40mm, central frequency of **75 MHz**, and a measured bandwidth of **65.5 MHz**, was estimated as **4000**. With the use of 3-inch optics, in contrast, is possible to realize the use of a TeO_2 acousto-optical cell with an effective aperture up to 60mm and the rest of the parameters from the previously used cell, potentially achieving time-bandwidth products (TMBP) of **6000.**

The estimation of the potential frequency resolution is as follows. Taking both cells as equals will have the same parameters, including the same TBWP. Suppose that one wants to analyze a signal with a bandwidth of **2GHz** , the frequency resolution would be 55 Hz using the appropriate chirp signals. For the previous version with 2-inch optics the resolution would have been around 125Hz, this means a total improvement of 125%

4.6. Conclusions

The analysis of the components for a 3-inch optics triple product processor is considered. Selecting top quality components for each part of the device and with the adequate characteristics to have the best possible performance. The proposed triple product processor has the capability of exploiting the larger window aperture than previous studies [4.8], around 60 mm, of a potential acousto-optical cell made of tellurium dioxide, previously studied with 2-inch optics and an acousto-optical cell with aperture of 40 mm, improving the time-bandwidth product about 50% on each cell, having with this, an improvement of 125% in spectral resolution which shows a great potential for is application in astrophysical spectroscopy.

Chapter 5

General Conclusions

The inefficient situation in the Guillermo Haro observatory, related to the need of changing diffraction gratings, can be solved. An alternative for the static diffraction gratings is the use of specially designed acousto-optical cell as a dynamic (i.e. completely electronically tunable) diffraction grating, whose capabilities will make it possible in the nearest future to replace all the static diffraction gratings from the spectrometer. The principal advantages of similar dynamic acousto-optical grating are excluding any mechanical operations within the observation process, avoiding recalibrations (i.e. bringing in additional errors) and any losses of time. The design of a desirable acousto-optical cell, adequate to this problem, have been proposed and analyzed

Now, it is possible to predict that a specific mechanism of the acousto-optic nonlinearity is capable of regulate performances of the existent collinear acousto-optical filter and can be used practically. The analysis of this mechanism has been made theoretically and has been confirmed experimentally with an advanced filter based on calcium molybdate ($CaMoO_4$) single-crystal and governed by external signals of finite amplitude.

The previous performed estimations which showed that the algorithm of space-and-time integrating was definitely suitable for a wideband spectrum analysis were taken into account and the design of a new triple product processor with an ultimate frequency resolution has been made. This algorithm uses an advanced acousto-optical processor to produce the folded spectrum of those signals, accumulating advantages of space and time integrating. The developing of a schematic arrangement for the triple product acousto-optical processor based on 3-inch optical components of a top-level quality have been made and the estimations show an improvement of 125% in the spectral resolution with respect to the previous considered system.

Future work

The work presented in this thesis can be continued in several ways. First, the use of an acousto-optical dynamic grating leads to infinite possibilities in its arrangement, starting from the use of different kinds of acousto-optical cells to the possibility to search for new materials with better properties. Also it can be focused on other spectra; it is not limited to the visible range. Another possibility is the use of more than one cell to use another kind of spectral analysis. The next thing to do, almost applicable immediately, is the use of several frequencies at the same time in the cell. This will generate several diffraction gratings simultaneously and potentially it will bring more advantages to the spectrometer.

After the study of the filter in a lossless medium, the next thing to do is to make the same analysis but having in consideration the acoustic losses in the medium of interaction and study the behavior of the transmission function and other properties in the collinear acousto-optical filter. Also it is reasonable to analyze other tunable acousto-optical filters based on different materials.

Related to the triple product processor, the next step would be the realization of the prototype to study its capabilities experimentally for its direct application in astrophysical spectrum analysis. Another way to continue the developing of this device would be to extend the study, previously done, of new materials for its use in the acousto-optical cells.

Bibliography

Chapter 1

[1.1] A. Korpel, Acousto-Optics, 2nd. Ed., Marcel Dekker, New York, (1997).

[1.2] A. Yariv & P. Yeh, Optical Waves in Crystals, John Wiley & Sons (1983).

[1.3] J. E. B. Oliveira, C.K. Jen, Backward collinear acoustooptic interactions in bulk materials, Applied Optics Vol. 29 No. 6 (1990).

[1.4] C. Kittel, "Introduction to Solid State Physics", 8th. Ed., John Wiley & Sons, New York, (2004).

[1.5] D.A. Pinnow. "Guidelines for the selection of acousto-optic materials." IEEE Journal of Quantum Electronics. Vol.QE-6 (1970), 223-238.

[1.6] T. M. Smith, A. Korpel, "Measurement of light-sound interaction efficiencies in solids", vol. QE-1 (1965), 283 -284.

[1.7] E. I. Gordon, "Figure of merit for acousto-optical deflection and modulation devices", IEEE J. Quantum Electronics, vol. QE-2, (1966), 104-105.

[1.8] R.W. Dixon, "Acoustic diffraction of light in anisotropic media", IEEE J. of Quantum Electronics. Vol.QE-3, no.2 (1967), 85-93.

Chapter 2

[2.1] Yu. I. Sirotin and M. P. Shaskolskaya. [Fundamentals of Crystal Physics], Mir Publishers. Moscow, (1982).

[2.2] A. I. Akhieser. Soviet Physics: Journal of Experimental and Theoretical Physics. vol.8, p.1318 (1938).

[2.3] N. Uchida and N. Niizeki. “Acousto-optic deflection materials and techniques.” Proc. IEEE. Vol.61, 1073-1092 (1973), 1073-1092.

[2.4] V. G. Dmitriev, G. G. Gurzadyan, and D. N. Nikogosyan. [Handbook of nonlinear optical crystals]. Springer-Verlag, New-York, 1999.

[2.5] A. A. Blistanov. [Crystals for Quantum and Nonlinear Optics], 2-nd. Ed., MISIS Publisher, Moscow, 2007.

[2.6] R. W. Klein and B. D. Cook. "A unified approach to ultrasonic light diffraction.", IEEE Transactions of Sonics and Ultrasonics, vol. SU-14, no. 3, (1967), 123-134.

[2.7] V. I. Balakshy, V. N. Parygin, and L. E. Chirkov. [Physical Principles of Acousto-Optics], Radio i Svyaz Press, Moscow, 1985.

[2.8] J. W. Goodman. “Introduction to Fourier Optics”, 3-rd Ed., Roberts & Co., Greenwood Village, USA 2005.

[2.9] M. B. Vinogradova, O. V. Rudenko, and A.P. Sukhorukov. “The Wave Theory”, Nauka Publishers. Moscow, 1990.

[2.10] E. I. Gordon. "A review of acousto-optical deflection and modulation devices." Proc. IEEE, Vol.54, no.10, 1966, pp.1391-1401.

[2.11] D. H. McMahon. "Relative efficiency of optical Bragg diffraction as a function of interaction geometry." IEEE Transactions Sonics & Ultrasonics. Vol.SU-16, no.2, 1969, pp.41-44.

[2.12] A. S. Shcherbakov, **A. O. Arellanes Bernabe**, V. Chavushyan, “Designing the acousto-optical cell for optical spectrometer incorporated into the Guillermo Haro astrophysical observatory”, Proc. Of SPIE vol. 8855-6, (2013), (To be published)

[2.13] A. S. Shcherbakov, **A. O. Arellanes Bernabe**, V. Chavushyan, “Designing an acousto-optical spectrometer for Guillermo Haro astrophysical observatory”, Proc. Of SPIE vol. 8842-22, (2013), (To be published).

Chapter 3

[3.1] J.L. Bertaux, D. Fonteyn, O. Korablev, at al. “SPICAM: Studying the global structure and composition of the martian atmosphere.” In European Space Agency; SP-1240 “Mars Express: A European mission to the red planet.” Edited by A. Wilson, ESA Publications Division, (2004).

[3.2] J.L. Bertaux, D. Nevejans, O. Korablev, at al. “SPICAV on Venus Express: Three spectrometers to study the global structure and composition of the Venus atmosphere.” Planetary and Space Science. Vol.55, issue 12, October (2007), 1673-1700.

[3.3] R.W. Dixon, “Acoustic diffraction of light in anisotropic media”, IEEE J. of Quantum Electronics. Vol.QE-3, no.2 (1967), 85-93.

[3.4] S.E. Harris, S.T.K. Nich, R.S. Fiegelson, “CaMoO4 electronically tunable optical filter”, Appl. Phys. Lett. Vol.17, no.5 (1970), 223-225.

[3.5] I.C. Chang, “Tunable acousto-optic filter utilizing acoustic beam walk-off in crystal quartz”, Appl. Phys. Lett. Vol.25, no.9 (1974), 323-324.

[3.6] J.A. Kusters, D.A. Wilson, D.L. Hammond, “Optimum crystal orientation for acoustically tuned optical filters”, J. Opt. Soc. Am. Vol.64, no.4 (1974), 434-440.

[3.7] E.T. Aksenov, N.A. Esepkina, A.S. Shcherbakov, “Acousto-optical filter with a LiNbO3-crystal” Tech. Phys. Lett, Vol.2, no.3 (1976), 83-84.

[3.8] J.D. Fichter, M. Gottlieb, J.J. Conroy. Appl. Phys. Lett. Vol.34, no.1 (1979), 1-3.

[3.9] V.I. Balakshy, V.N. Parygin, L.I. Chrkov. Physical Principles of Acousto-Optics, Radio I Svyaz, Moscow, (1985).

[3.10] A. Korpel. Acousto-Optics, 2-nd Ed., Marcel Dekker, New-York, (1997).

[3.11] F.T.S. Yu. Introduction to Information Optics, Academic Press, San Diego, (2001).

[3.12] A.S. Shcherbakov, A. Aguirre Lopez, “Shaping the optical components of solitary three-wave weakly coupled states in a two-mode waveguide”, Optics Express. Vol.11, no.14 (2003), 1643-1649.

[3.13] A.S. Shcherbakov, A. Aguirre Lopez, “Binary encoded modulation of light based on collinear three-wave acousto-optical weakly coupled states”, Journal of Optics A: Pure and Applied Optics. Vol.5 (2003), 471-477.

[3.14] Yu.I. Sirotin and M.P. Shaskolskaya. Fundamentals of Crystal Physics, Mir Publishers. Moscow. (1982).

[3.15] V.G. Dmitriev, G.G. Gurzadyan and D.N. Nikogosyan, Handbook of Nonlinear Optical Crystals 3-rd Ed., Springer, Berlin, (1999).

[3.16] A.A. Blistanov. Crystals for Quantum and Nonlinear Optics. 2-nd Ed., MISIS, Moscow, (2007).

[3.17] D.A. Pinnow. “Guidelines for the selection of acousto-optic materials.” IEEE Journal of Quantum Electronics. Vol.QE-6 (1970) 223-238.

[3.18] Handbook “Acoustical Crystals”. Edited by M.P. Shaskolskaya. Nauka Publishers, Moscow. (1988).

[3.19] A. S. Shcherbakov; **A. O. Arellanes**; S. A. Nemov “Transmission function of the collinear acousto-optical filter controlled by acoustic waves of the finite amplitude”, Optical Engineering vol. 52, no. 06, 064001,(2013)

Chapter 4

[4.1] P. Kellman. “Time integrating optical processing.” Ph. D. thesis. Stanford University (1979).

[4.2] Terry M. Turpin, “Time integrating optical processors”, SPIE Vol. 154 (1978), 196-203.

[4.3] Robert M. Montgomery, US Patent 3634, 749, filed 15 July (1970)

[4.4] Goutzoulis A., Pape D., Design and fabrication of acousto-optic devices, Marcel Dekker, New York, (1994)

[4.5] Anthony Vanderlugth, Optical Signal Processing, John Wiley & Sons (1992)

[4.6] Abdul J. Jerry, “The Shannon Sampling Theorem-Its Various Extensions and Applications: A Tutorial Review”, Proceedings of th IEEE, Vol 65, No. 11, (1977), 1565 – 1596.

[4.7] Joseph T. Verdeyen, Laser Electronics, 3rd. Edition, Prentice Hall (1995)

[4.8] A. V. Hanessian, “Designing the prototype of acousto-optic processor for astrophysical applications”, M. Sc. thesis, INAOE, (2012)

Statements

1. A new dynamic diffraction grating realized by specially designed acousto-optical cell could be potentially exploited as a dispersive element within uses an optical spectrometer for The Guillermo Haro astrophysical observatory. Such a dynamic (i.e. completely electronically tunable) diffraction grating represents an alternative for a set of traditional static diffraction gratings. The principal advantages of similar dynamic acousto-optical grating are excluding any mechanical operations within the observation process, avoiding recalibrations (i.e. bringing in additional errors together with losses of time), and improving the efficiency of spectrum analysis.

2. A specific mechanism of the acousto-optic nonlinearity, being capable to regulate performances of the collinear acousto-optical filter, exists and could be used practically when an advanced filter is governed by external electronic signals of finite amplitude.

3. The algorithm of space-and-time integrating could be suitable for a wideband spectrum analysis with an ultimate frequency resolution. This algorithm requires an advanced acousto-optical processor to produce the folded spectrum of those signals, accumulating advantages of space and time integrating. The suggested schematic arrangement for the triple product acousto-optical processor, based on three-inch optical components of a top-level quality, can be designed.